

University of Mississippi

eGrove

Electronic Theses and Dissertations

Graduate School

1-1-2014

Finite element analysis of shear resistant mechanisms for biolaminate interfaces

Matthew Nelms

University of Mississippi

Follow this and additional works at: <https://egrove.olemiss.edu/etd>



Part of the [Mechanical Engineering Commons](#)

Recommended Citation

Nelms, Matthew, "Finite element analysis of shear resistant mechanisms for biolaminate interfaces" (2014). *Electronic Theses and Dissertations*. 1329.

<https://egrove.olemiss.edu/etd/1329>

This Dissertation is brought to you for free and open access by the Graduate School at eGrove. It has been accepted for inclusion in Electronic Theses and Dissertations by an authorized administrator of eGrove. For more information, please contact egrove@olemiss.edu.

**FINITE ELEMENT ANALYSIS OF SHEAR RESISTANT MECHANISMS FOR
BIOLAMINATE INTERFACES**

A Thesis
Presented in partial fulfillment of requirements
For the degree of Master of Science
in the Department of Mechanical Engineering
The University of Mississippi

By
Matthew Nelms

December 2014

ABSTRACT

The Alligator gar possesses a flexible dermal armor consisting of overlapping ganoid scales. Each scale is a bilayer hydroxyapatite and collagen-based bio-laminate for protection against predation. The exoskeleton fish scale is comprised of a stiff outer ganoine layer, a characteristic “sawtooth” pattern at the interface and a compliant bone inner layer with all materials exhibiting a decreasing elastic modulus, yield strength and density through the thickness. Experiments on ganoid scales revealed properties such as damage mitigation and energy dissipation that are unique to biological dermal armor.

The objective of this investigation is to develop a fundamental understanding of the stress response of a fish scale under tensile and shear loading conditions and to compute effective elastic properties. The effects of material grading and the influence of the geometrically and materially nonlinear interface between the ganoine and bone layers on the elastic properties were also considered. A three dimensional finite element method (FEM) was used by employing ABAQUS® code. The current work also investigated possible mechanisms associated with delamination resistance and energy dissipation of the bio-laminate structures. The model structure for the fish scale in the FEM was Alligator gar.

The finite element analysis (FEA) is based on a microscopic representative volume element (RVE) of the fish scale with an overall thickness of 800 micron. The FEA RVE had one million uniform 8-micron cubical 8-node elements. The geometrically nonlinear sawtooth features are explicitly modeled. An elastic-plastic model described the nonlinear material

response. The analysis focused on evaluating the nonlinear material response in terms of energy dissipation and stress redistribution at the ganoine-bone interface. The results indicate that a complex redistribution of stresses across the 800 micron thickness occurred due to functional gradation of properties, from the stiff mineralized ganoine to the soft bone layer. While the stress concentration was limited to the interface between the saw tooth and the surrounding bone layer, the average stresses in the ganoine layer were much lower as compared to the distributions in the bone layer. The internal energy at the ganoine-bone interface is reduced and energy is dissipated across the sawtooth junction points.

Keywords: Biological Materials, Delamination Resistance, Alligator gar, Energy Dissipation

DEDICATION

This thesis is dedicated to my wife, family and friends. All of which have provided the support and patience to make this journey possible.

LIST OF ABBREVIATIONS

FEA	Finite Element Analysis
RVE	Representative Volume Element
KBC	Kinematic Boundary Condition
PBC	Periodic Boundary Condition
2D	Two Dimensional
3D	Three Dimensional
HAp	Hydroxyapatite
GPa	Gigapascal
MPa	Megapascal
σ	Stress
ε	Strain
U	Strain Energy
V	Volume
E	Young's Modulus

ACKNOWLEDGMENTS

I would like to first thank my advisor Dr. A.M. Rajendran for allowing me to take on such an exciting project. His guidance, support, insights, and, particularly, his mentorship proved to be invaluable to producing this thesis.

I would like to express my gratitude toward Mr. Wayne Hodo of U.S. Army ERDC at Vicksburg, MS for the many conversations about my research. His technical guidance and constant forethought has allowed for my personal and professional growth, which allowed me to complete research project. My research was in support of the U.S. Army ERDC Military Engineering 6.1-ILIR Basic Research Project on “Investigation of Delamination Resistant Bio-Laminates “. The effort was funded by the U.S. Army Research Office’s PIRT Program under Contract No. W911NF-11-2-0043.

Last, but certainly not least, I would like to thank Dr. Tez Tadepalli for his aid with ABAQUS® Finite Element Software and the many discussions related to representative volume element modeling. His time and knowledge were crucial to the completion of the project.

TABLE OF CONTENTS

ABSTRACT.....	ii
DEDICATION.....	iv
LIST OF ABBREVIATIONS.....	v
ACKNOWLEDGMENTS.....	vi
TABLE OF TABLES.....	x
TABLE OF FIGURES.....	xi
CHAPTER 1: INTRODUCTION.....	1
CHAPTER 2: BACKGROUND	4
2.1 Fish scale Macro, Meso, Micro and Nanostructures	6
2.2 Basic fish scale macrostructures and FE modeling.....	6
2.3 Fish scale substructures – progressing down the length scales.....	10
2.4 Fish scale Protein: Collagen fibers	12
2.6 Biomineral Hydroxyapatite.....	15
CHAPTER 3: STRENGTHENING AND ENERGY DISSIPATION MECHANISMS	17
3.1 Geometrically interlocked interface.....	17
3.2 Functional Grading of Material Properties	18

3.3 Delamination resistance	20
3.4 Hydration effects on mechanical behavior	21
CHAPTER 4: METHODOLOGY	23
4.1 Generation of RVE Model	23
4.2 Representative volume element	24
4.3 Functional Gradation for RVE simulations	26
4.4 Geometrically interlocked interface.....	27
4.5 Boundary Conditions	28
CHAPTER 5: FINITE ELEMENT ANALYSIS RESULTS	30
5.1 ABAQUS® Simulation Results.....	30
5.3 Stress distribution due to structured interface and functional graded material properties..	32
5.3 Structured interface under shear loading conditions.....	37
5.4 Elastic Energy Dissipation.....	40
5.4 Elastic - Perfectly Plastic Compression simulations.....	43
CHAPTER 6: CONCLUSIONS AND FUTURE WORK	48
6.1 Conclusions	48
6.2 Future Work	49
LIST OF REFERENCES.....	50

LIST OF APPENDICES	57
APPENDIX A: PYTHON SCRIPT FOR ABAQUS ODB FILE.....	58
APPENDIX B: PARAVIEW STRESS PLOTS.....	64
APPENDIX C: ABAQUS® SCALABILITY	67
VITA.....	70

TABLE OF TABLES

Table 1: RVE layers and property grading for Alligator gar fish scale	25
Table 2: Effective macroscale properties for Alligator gar fish scale RVE - Sawtooth	32
Table 3: Effective macroscale properties for Alligator gar fish scale RVE - Planar	32
Table 4: Strain energy density for the ganoine and bone layers	40
Table 5: Elastic and plastic energy dissipation	46
Table 6: ABAQUS® Scalability for one million element Alligator gar RVE.....	68

TABLE OF FIGURES

Figure 1: Toughness of current engineering and the hierarchal structures in osseous biosystems .	2
Figure 2: Fish scale classification types.....	7
Figure 3: Fish scale lay-up.....	8
Figure 4: Alligator gar meso and microstructure and Gray bichir.....	10
Figure 5: Mechanical anisotropy of HAp pillar and HAp nanocrystal.....	11
Figure 6: Collagen structure hierarchy	13
Figure 7: Stress reduction at decreasing length scales.....	14
Figure 8: Stress strain curve for HAp for various size MD specimens	15
Figure 9: SEM image of the "sawtooth" structure ganoine bone interface.....	17
Figure 10: Hierarchal structure present in Alligator gar fish scale.....	18
Figure 11: Material property variations in Alligator gar fish scale	19
Figure 12: Functional grading of Gray bichir fish scale	20
Figure 13: Delamination resistance of Alligator gar during indentation testing	20
Figure 14: Tensile Response of dehydrated and hydrated Alligator Gar fish scales	22
Figure 15: One million element RVE mesh.....	24
Figure 16: ABAQUS [®] RVE of functionally graded material model.....	25
Figure 17: RVE functional grading intensity plot of elastic modulus for representative layer	27
Figure 18: RVE functional grading intensity plot of elastic modulus for sawtooth intrusion.....	28
Figure 19: Kinematic boundary conditions: uniaxial and shear displacement conditions.....	29
Figure 20: RVE stress distribution under uniaxial displace condition with the sawtooth(u_{11}).....	33

Figure 21: Normalized stress in the ganoine for Alligator gar under uniaxial loading conditions	34
Figure 22: Normalized stress in the ganoine for Alligator gar under uniaxial loading conditions	35
Figure 23: RVE stress distribution under uniaxial displacement condition without the sawtooth	36
Figure 24: Shear stress response of Alligator gar fish scale	37
Figure 25: RVE stress distribution under uniaxial displacement condition	38
Figure 26: Normalized stress at the interface for sawtooth interlocked model	39
Figure 27: Strain energy density for u_{11} displacement condition	41
Figure 28: Strain energy density for u_{22} displacement condition	42
Figure 29: Strain energy density for u_{33} displacement condition	43
Figure 30: Strain energy density for u_{12} displacement condition	43
Figure 31: Stress-strain curves for various elements in the interface layer	44
Figure 32: Plastic energy dissipation for single sawtooth model of Alligator gar interface.....	45
Figure 33: Elastic - perfectly plastic simulation results for the one million element RVE	46
Figure 34: RVE energy dissipation during compression loading	47
Figure 35: RVE stress distribution under uniaxial displacement condition (u_{22})	65
Figure 36: RVE stress distribution under uniaxial displacement condition (u_{33})	66
Figure 37: ABAQUS [®] scalability versus ideal for one million element RVE	68

CHAPTER 1

INTRODUCTION

Biological materials (biomaterials) have had a marked increase in interest from the material science and engineering community due to unique characteristics and properties that are typically sought after in traditional engineering materials. Biomaterials are materials related to living organisms and the basis for abstracting characteristics for bio-inspired design [1-26]. Of recent interest is the mechanical response of various fish scale structures [27-44]. Previously the research into osseous materials had been primarily focused on human and bovine bone [45-58] and the micro-constituents [59-93]. Unlike metals, ceramics, and traditional composite materials; biomaterials often possess enhanced characteristics such as, penetration resistance [2-3], high toughness, flaw tolerance [13,21], energy dissipation [10], damage mitigation [34], and delamination resistance [34,44] all while achieving high strength-to-weight ratios. Buehler defined robustness as “the ability of a material to tolerate flaws and defects in its structural makeup while maintaining its ability to provide functionality” [9]. Biomaterials exhibit the robustness desired in advanced material systems and provided a basis for future material design. Biomaterials such as fish scale exoskeletons, bone, antler exhibit high toughness and stiffness response (Figure 1). Given this desired combination, these bio-systems are being investigated for bio-inspired design of new material systems [2-3].

Biological materials (biomaterials) often contain a more structured hierarchy from macro- to nanoscale [19,23,25] that is not currently possible with today's engineering composites. The robust mechanical behavior has caused an increasing interest in biomaterial modeling and bio-inspired design of advanced material systems [8]. With this comes a need for the development of theoretical mechanics and the computational methods that aid in the understanding of such diverse biomaterials that otherwise cannot be determined from physical experiments.

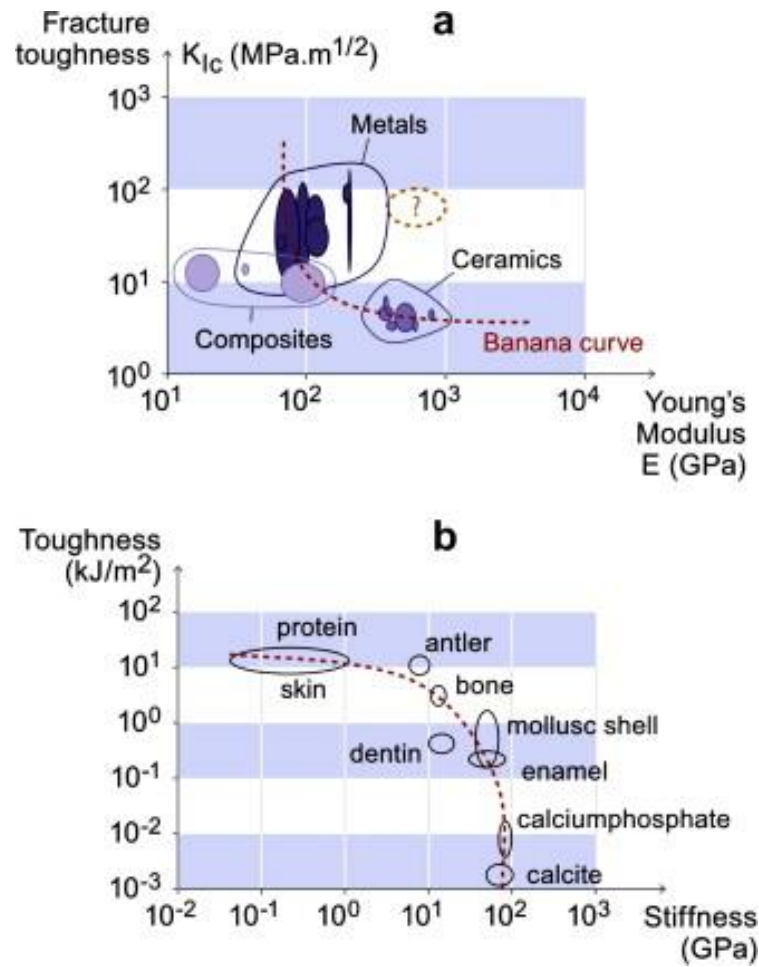


Figure 1: Toughness of current engineering (a) and the hierarchal structures in osseous biosystems (b) [22]

The focus of this research is the computational modeling of Alligator gar (*Atractosteus spatulas*) fish scales. The model scheme employed ABAQUS[®] Finite Element Analysis (FEA) software and a novel 3D representative volume element (RVE) based approach that includes

functional grading of material properties, structured interface and elastic – perfectly plastic material behavior to determine elastic properties, effective mechanical response of the unit cell and strain energy dissipation for both kinematic and periodic boundary conditions.

Chapter 2 details the background on fish scale characteristics and other related multiscale features. The strengthening and energy based mechanisms are discussed in Chapter 3. Chapter 4 discusses the mesoscopic finite element modeling of the fish scale focusing on the basis for discretization as well as the mathematical basis for describing the functional gradation of properties in a microscopic RVE constructed for ABAQUS[®]. A stress analysis based FEA results are presented in Chapter 5. The complex redistribution of stresses across the thickness of the fish scale due to various interfaces, including the sawtooth feature, and the energy dissipation mechanisms are discussed in this section. Chapter 6 summarizes the salient findings from the detailed FEA.

CHAPTER 2

BACKGROUND

The review consists of fish scale and related biocomposite materials, beginning with the general overview, material structure at various scales, and mechanical properties. This section provides a brief introduction to the physical structure of the constituent materials and geometric aspects as related to the mechanical properties of biological materials response to external stimuli. The biomaterial descriptions are presented in decreasing scale starting at the macroscale and moves towards progressively smaller structures.

The research chosen for review is due its relation to biological mechanical modeling of fish scales. Starting with the most recent fish scale modeling research then onto the related computational and mathematical modeling related to collagen/HAp-based biocomposites. Interest in the computational modeling of fish scales is currently limited [30,32,33,38,43,44]. Thus, bone is also discussed as needed to provide a basis of direct mechanical and computational characterization of fish scale substructures and the necessary analogs due to similar hierarchal structure, mineral – protein composition and mechanical response. In addition, the review covers hydroxyapatite and collagen proteins as they pertain to fish scale modeling.

At the current moment there is little FEA performed on Alligator gar and other fish scales. The approach used by Bruet et al.[32] and Han et al. [38] on the Gray birchir as well as Chandler et al. on Alligator gar have used 2D axis-symmetric approach [44]. Bruet et al. [32]

focused on the effects functionally graded material properties. Han et al. [38] investigate the effects of HAp nanorod orientation on the mechanical properties of the ganoine layer. Chandler et al. [44] have employed a cohesive zone model to analyze potential delamination at the ganoine-bone interface.

The current material models and FEM are based out of traditional linear elastic material descriptions. While this provides necessary insights into nanoscale material behavior it fails to capture the energy dissipative nature provided by viscoelastic material response observed during experimentation. Additionally, simplifications of geometry fail to describe the in-vivo structures present and the directional dependency of material response. Collagen fibers have been shown to aid in principal loading response and current efforts neglect the complex nanoscale 3-D geometric interactions of both collagen and HAP phases as well as hydration state effects on nonlinear response. Proteins have been tested and molecular dynamics (MD) simulations shown a hyperelastic/viscoelastic material behavior that is also not yet accounted for in current mechanical modeling. 2-D axis-symmetric modeling by Tai et al. [51] has shown the heterogeneous material make up aids in energy dissipation and 2-D simulations by Espinoza et al. [25] have shown strengthening by structural interlocking present and biomaterial interfaces. Still needed is a model to describe the concurrent anisotropic response present in both the biomineral and fibrous collagen phases. Current computational models also neglect variations in material properties with respect to location. Experimentation on bone, fish scale and nacre has shown preferentially varied material properties with consistent aspects such as functional gradation, structural and material anisotropy. The current computational modeling assumes consistent material properties and simplified elastic – perfectly plastic material behavior.

2.1 Fish scale Macro, Meso, Micro and Nanostructures

While the research presented is focused on the mesoscale structures it is necessary to discuss the underlying micro and nanoconstituents to fully describe fish scale and the complexity involved in accurate FEA simulations. Fish scales and other biomaterials have been of recent interest for their penetration resistance [33], flaw tolerant behavior [24], damage mitigation through ring cracking [34], crack arresting [24] for potential light weight biologically-based composite (biocomposite) design. Fish such as the Alligator Gar (*Atractosteus spatula*) [35-40,44] and Gray bichir (*Poly senegalus*) [2-3,33] have been researched due to their particular dermal armor characteristics and complex multilayer bicomposite structure. With the advent of additive manufacturing and 3-D printing technologies that approach the microscale they are emerging as a basis for force protection material and structures including research into articulating armor by Song in 2011 [2].

2.2 Basic fish scale macrostructures and FE modeling

Fish exoskeletons have been of recent interest due to their unique physical, chemical and engineering properties. Fish scales can be classified based on general characteristics in to elasmoid, ganoid, cosmoid, placoid [40-41] and dermal armor groups [2-3]. The primary difference between fish scale classifications being the volume fraction of each micro-constituent as well as the anisotropic structural and material arrangement effect on macroscale properties. The mineral component, hydroxyapatite (HAp), and the organic component, collagen fibers, are consistent throughout many fish scales and bone biomaterial systems with each showing distinct structures at all length scales [2-3,27-44].

Progressing from the most evolutionary modern fish scale to more primitive, the fish scale classifications are as follows: elasmoid, placoid, ganoid and cosmoid as well as a separate

category for specifically dermal armor (Figure 2). Current research has been on fish scales in the elasmoid and ganoid scales with expanded interest into the dermal armor of the threespine stickleback [2-3]. The general structure of fish scales will be present with particular reference made to these scale classifications.

Elasmoid fish scales are characterized as a “modern” fish scale. They are a bilayer bio-composite comprised of an external osseous (or bony) layer and a fibrillar internal layer. The external plate is primarily composed of the mineral hydroxyapatite and randomly oriented collagen fibers. The external layers are often described as “highly mineralized” due to the high hydroxyapatite content. The relative amount of mineralization is the primary distinctions between layers [17].

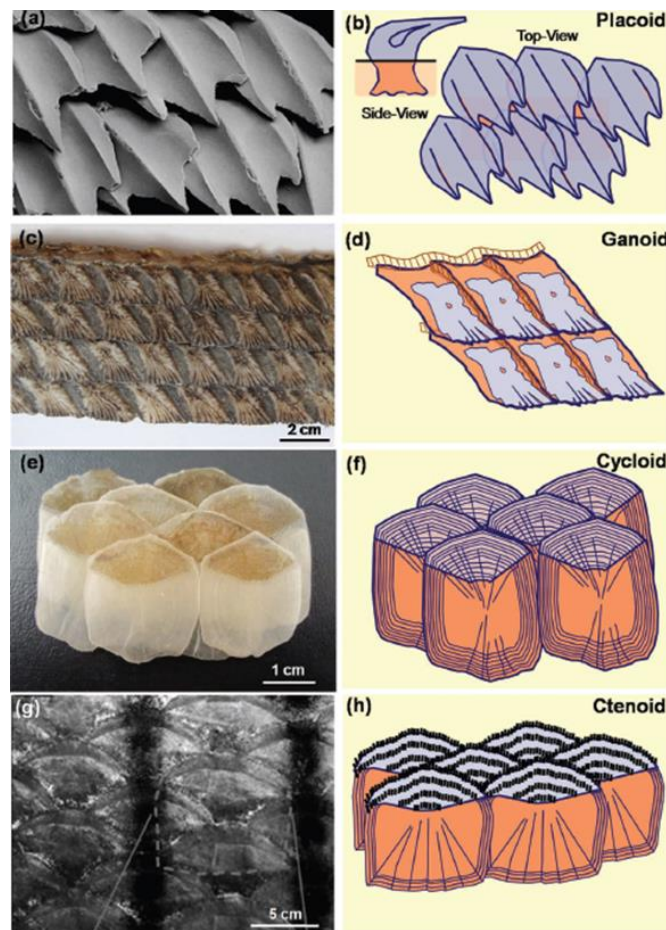


Figure 2: Fish scale classification types [40]

The species of teleost comprises 96% of all modern fish and most commonly have elasmoid scales. Specifically, scales from the teleost fish the striped bass (*Marone saxatilis*) have been researched for their bite or puncture resistance [30]. Teleost scales contain the least mineralized external layer of the fish scales reviewed. They can be divided into cycloid and ctenoid subtypes based on fibular orientation. Elasmoid fish the scales are completely embedded in an elastic protein matrix on both external and internal surfaces as seen in Figure 3.

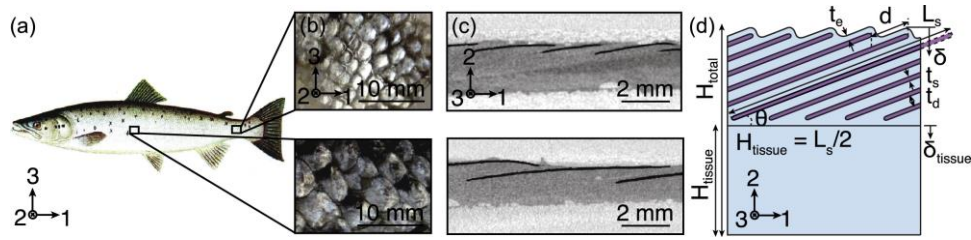


Figure 3: Fish scale lay-up [42]

Placoid scales are most commonly known from sharks and rays. They primarily consist of an osseous basal plate and dentin with an enameloid covered spine that protrudes through the epidermis. The primary function of these scales believed to be for hydrodynamic properties, abrasion resistance and some predator protection. Given their minimal strength and puncture resistance, they will not be reviewed in detail.

Ganoid scales are an evolution of the ancient (and extinct) cosmoid scales. The material structure as complex as the quadlayered biocomposite of *P. senegalus* where the lamellar structure is as follows (exterior to interior progression): highly mineralized external layer of ganoine, then the random, less mineralized structure of dentine, a lamellar bone structure of isopedine and a highly collagenous osseous inner layer (see Figure 3) [28-29]. Or as simple as the bilayer biocomposite of *A. spatula* with a ganoine layer covering 40 – 70% of the osseous basal plate layer (see Figure 3). This layering exhibits a functional grading of decreasing hardness under nanoindentation testing from the external towards the internal layers [31-33, 37].

The ‘functional grading’ is most drastic near the internal layers interfaces. In addition, the interfacial surfaces geometric complexity has been of interest into how it effects the stress distribution and contribution to overall material behavior has investigated Chen [37] in 2012.

Many researchers have reported plywood-like layup with the collagen fiber angle varying from layer to layer. For some fish a Bouilgand (a varying helical fiber orientation) structure has been reported [27-28,36-37,39-40], leading to increased complexity in the biocomposite lamellar structure.

Compared to the elasmoid scale, ganoid scales are considered a more primitive variation of fish scales and the extra layers provide increased puncture resistance. The current research in ganoid fish scales has primarily focused on, *Polypterus senegalus* (gray bichir) [31], *Arapaima* (*Arapaima gigas*) [36-37,39-40] and Alligator gar (*Atractosteus spatula*) [34,35,44] due to the armor like characteristics of the ‘ancient’ scale [2-3,32].

Cosmoid fish scales are only found on extinct species, but are similar in structure to ganoid scales. The external layer is the enamel-like material vitrodentine (similar to ganoine), followed by cosmine (a dentine-like material), then two basal layers, one of spongy bone and the inner most layer being isopedine. Like the ganoid, cosmoid scales have a layered structure with a functionally graded composition.

Lastly, there are some fish exhibiting what is designated as dermal armor since the primary function is flexible armor against predators. Due to the specific evolution of the plates as a dermal armor, the *Gasterosteus aculeatus* (threespine stickleback) has been in recent research [2-3]. The armor plates of *G. aculeatus* consisting of primarily (58 – 68%) the biomineral HAp as well as being highly porous (20 – 35%). Song et al. [2-3] printed scaled up models to better understand the mechanics and articulating structure of the dermal armor.

2.3 Fish scale substructures – progressing down the length scales

The layering of fish scales is typically a thin highly mineralized external layer with decreasing mineralization and increasing compliance in the medial direction. Ganoid scales are typically rhombic in shape with variations in size and thickness (including internal layers) between location and species. In the case of the *P. senegalus*, the scales contain four layers. From external to internal the layers are ganoine, dentine, isopedine and an osseous basal plate [31]. For the Alligator gar, the scale has two layers with a functionally graded transition zone [34-35]. The external layer is ganoine covering 40 – 70% of the osseous basal plate [36-37].

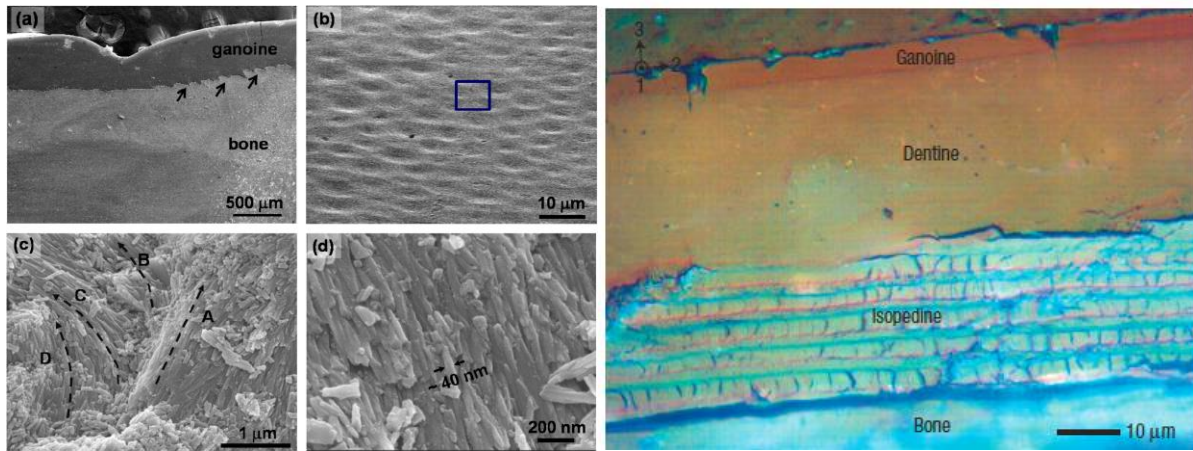


Figure 4: Alligator gar meso and microstructure (left) [35] and Gray bichir (right) [32]

In the case of ganoine, highly mineralized means >95% inorganic material. Ganoine is an enameloid material meaning enamel-like in composition with a pseudoprismatic hexagonal nanorod structure. Quantification of HAp pillar properties using compression testing (left) displays anisotropic behavior as do HAp single crystals (right). Han et al. [63] performed 2D axis-symmetric FE simulations to determine the effect of pillar orientation on the effective material properties and orthotropic behavior for the ganoine layer.

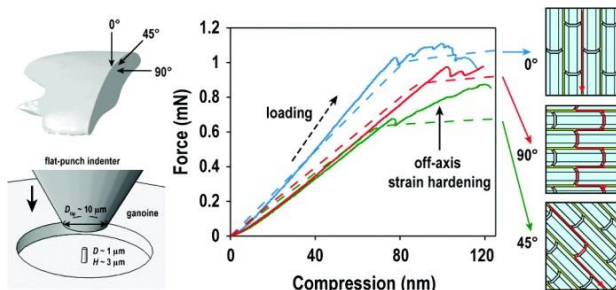


Figure 5: Mechanical anisotropy of HAp pillar (left) [38] and HAp nanocrystal (right) [63]

Within the mineral crystal pores are interstitial proteins. The ganoine layer is similar to ceramic in behavior being strong, hard, and the mechanical failure being brittle in nature. It is also the thinnest layer, for example, the alligator gar has a ganoine layer $\sim 50 \mu\text{m}$ as compared to the $\sim 750 \mu\text{m}$. *P. senegalus* was measured to $\sim 10 \text{ mm}$ making $\frac{1}{4}$ of the next thinnest layer. Using micro and nanoindentation testing the Young's modulus ranged from 55 to 80+ GPa [34,37].

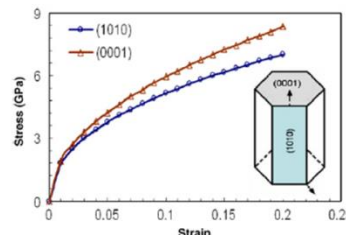


Fig. 3 – Stress-strain response of the hydroxyapatite single crystal extracted from nanoindentation data.

Progressing towards the internal layers next to the ganoine layer is dentine. The dentine has a significantly reduced HAp mineral content ($\sim 50\%$), increased organic content ($\sim 30\%$) with the organic phase being primarily mineralized collagen, and the rest being an interstitial fluid. The dentine in fish scale is congruent with tooth dentine. The dentine layer in the *Polypterus senegalus* was measured by Bruet et al. [31] to be $50 \mu\text{m}$. Isodepine exhibiting a more lamellar structure than dentine and the interior layer being comprised of porous bone. Primitive species such as the Alligator gar (*Atractosteus spatula*) are of interest for their more robust protection (Figure 1a). The genome of the Alligator garfish scale is comprised of collagen proteins and hydroxyapatite (HAp) minerals [34]. The exoskeleton structure consists of a bi-layered structure exhibiting a brittle ganoine outer layer (Figure 1b), characteristic “sawtooth” interlocking pattern between layers (Figure 1c), functionally graded interface and a soft bone inner layer [33,36-39]. The fish exhibit a more progressive grading of material properties and complex structure within each layer as well as more randomly interlocked interface [33,37,39].

2.4 Fish scale Protein: Collagen fibers

There are 28 different types of collagen with types I – III being the most abundant. In addition both Type I and Type II collagen have been shown to be structural supporting materials in bone and cartilage. Fibrous collagen is the protein mesostructures that are found in fish scales' bone and is known for its superior mechanical properties [70]. Fish scale collagen hierarchical structure, like most collagen, has a helical structure.

It is not quite clear how the HAp and collagen are structurally arranged in the exoskeleton fish scale. However, in lieu of providing a detailed description of the fish scale the analogue of collagen found in human bone will be discussed. The collagen found in human bone are mineralized fibers. Meaning they have transverse periodic HAp bands (~67 nm) that reinforce the fibers over their entire length. The mineralized fibers appear to be bonded by an unmineralized organic matrix [68], which consistent with in bone.

Type I Collagen fibers are made up of tropocollagen (TC) molecules bonded together in a triple helix [22] seems to play an important role in collagen's mesoscopic properties. TC fibrils have a diameter of approximately 1.1- 1.5 nm and length of 300 nm [22-23] which combine to form collagen microfibrils.

A completely unfolded TC molecule having a young's modulus of approximately 4 GPa at 8% strain [79]. TC molecules contain more than 1000 amino acids with glycine, proline and hydroxyproline being the primary residues found in collagen. Glycine has been found to have a near consistent periodicity every third molecule. Due to glycine occurs every third residue and allows for close inter-chain hydrogen bonding as well as chain to chain bonding necessary to form the collagen triple helix [70]. Collagen, tropocollagen and the related intermolecular forces

have been much of the focus for biomechanical modeling primarily through molecular dynamics and atomistic approaches to determine the properties of a single collagen fiber, TC molecule and intermolecular interactions.

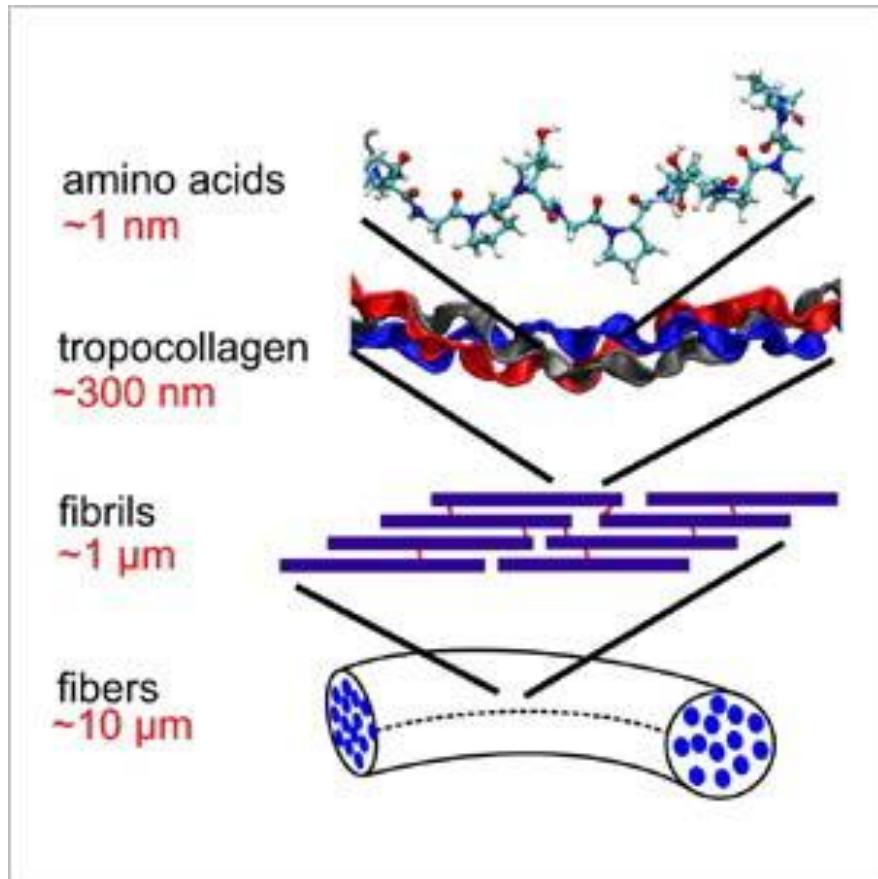


Figure 6: Collagen structure hierarchy [22]

The shearing mechanism from experimental testing has been found by Gupta et al. [16-17] to be consistent with the lap-joint model and highlights the importance of the fiber-matrix interface to the material performance. Collagen fibers also have exhibited sacrificial bonds between fibers and the fibril strain has been found to half the tissue strain suggesting shearing occurs in the interfibrillar matrix layers [16-17]. Figure 7 shows how the stress decreases with a decrease in hierarchal level. The difference in stress underscores the importance of understand the mechanical behavior of the microconstituents and bridging all length scales.

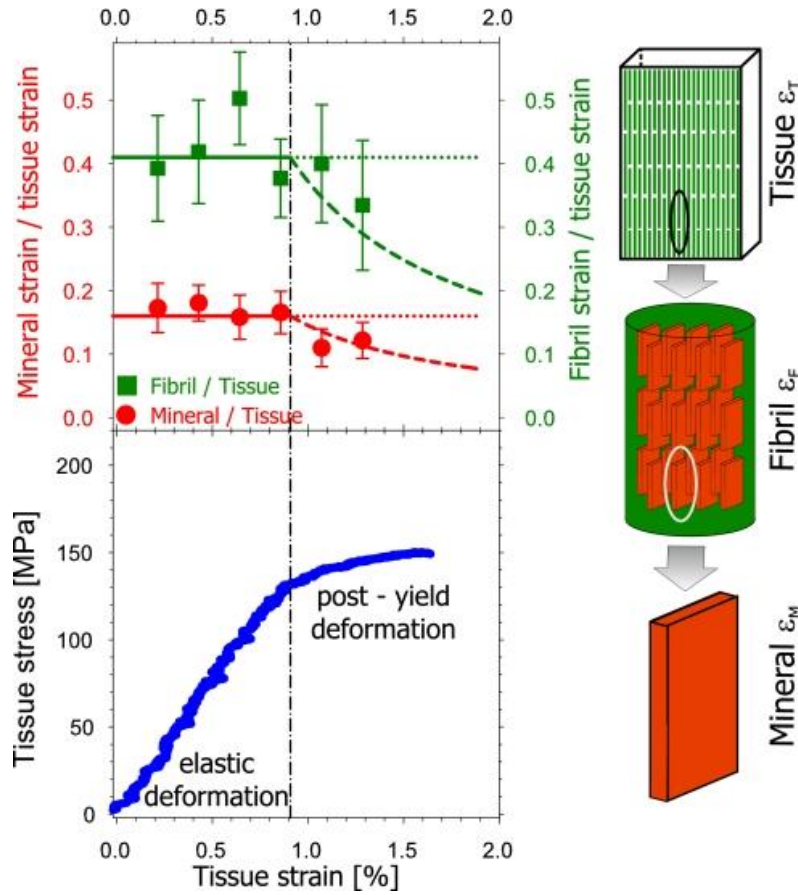


Figure 7: Stress reduction at decreasing length scales [17]

The tissue level being the macroscopic combination of primarily collagen fibrils, HAp platelets and extrafibrillar matrix (proteoglycans and other non-collagenous proteins). At small strains (less than 2%) the mechanical resistance is primarily due to intramolecular phenomena (molecular elongation or protein unfolding) and 0.3% has been attributed to intermolecular mechanisms (slippage and fiber gap increase). This appears analogous to fiber pullout exhibited in fibrous materials such as Kevlar. Failure of protein is defined when the main chain breaks. It also illustrates the need for a deep physical understanding of protein unfolding and intramolecular interactions to accurately capture the unique fiber behavior present in proteins such as collagen and the interaction with the surrounding biomineral hydroxyapatite (HAp).

2.6 Biomineral Hydroxyapatite

Bone found in fish scales are a hierarchal structure consisting of the biomineral carbonated calcium phosphate, HAp, and soft organic phase made up of primarily Type I –Type II collagen fibers. Biominerals are minerals produced by biological systems that typically exhibit brittle failure characteristics as seen in Figure 8 for HAp specimens of various size, have a highly organized crystalline structure and specifically in the case of HAp used in structural applications.

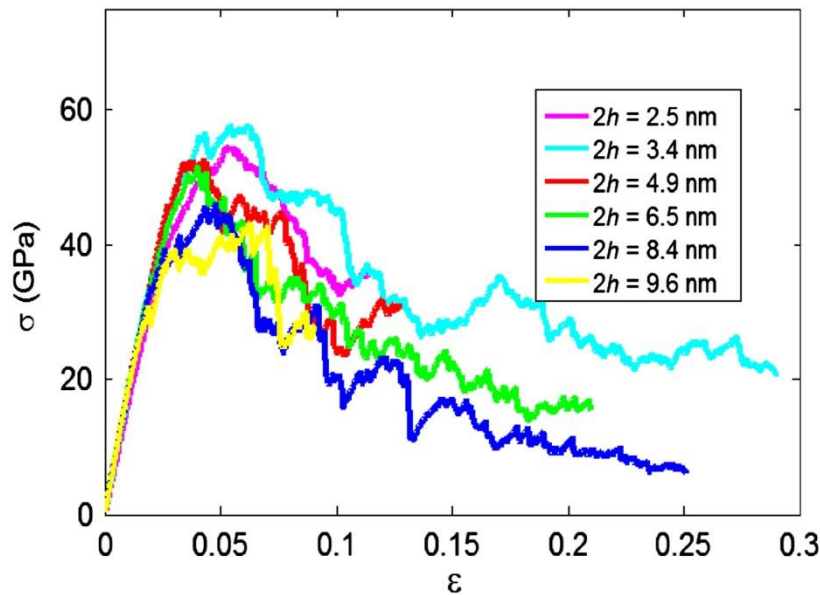


Figure 8: Stress strain curve for HAp for various size MD specimens [62]

Gao and Ji [19] have investigated the flaw tolerant design and modeling using fracture mechanics to develop a critical length scale defined as the maximum length scale that materials behave near theoretical strength. HAp exhibits a flaw tolerant behavior and performs at a near theoretical strength at scales much larger (200 – 400 angstroms) than those found in carbon nanotubes (0.2 angstroms) [5]. The mechanical stability has been attributed in part to the geometric confinement of HAp platelets in bone biomaterials [13,21].

The mineral phase is in bone mostly calcium hydroxyapatite with 4 – 6% by weight of the phosphate ions being replaced by carbonate ions. Hydroxyapatite or HAp is the primary

component in bone with a molecular composition of $\text{Ca}_5(\text{PO}_4)_3\text{OH}$. HAp in fish scale is a calcium deficient calcium phosphate that forms microscale mineral structures in mesoscale structures depending on the biological systems. On the microscale, the structures vary from species to species Yang et al. in 2012 [35] reported hexagonal nanorods from the Alligator gar ganoine having a 40 nm diameter and 220 nm (aspect ratio 5.5). Hardness testing of HAp single crystals by Saber-Samandari [92] found Young's modulus values of 143 – 155 GPa. Like fish scales, bone exhibits the same mineralized collagen fibers. The mineralization of collagen highlights the complex interaction of the mineral and protein phase and the difficulty in accurate characterization and modeling.

Apatite minerals often have a hexagonal dipyramidal crystalline structure [64]. HAp has been reported to monoclinic rather than hexagonal. The change in symmetry affects the microscale crystal structure thereby influencing the macroscale mechanical properties of the mineral phase. The minerals are found to be porous and contain interstitial proteinaceous material adding the multiscale structural complexity.

CHAPTER 3

STRENGTHENING AND ENERGY DISSIPATION MECHANISMS

3.1 Geometrically interlocked interface

Alligator garfish scales exhibit a geometrically interlocked interface between the stiff ganoine outer layer and the compliant bone inner layer. The interface exhibits a distinct periodic sawtooth structure with the ganoine layer intruding into the interfacial region of the fish scale. [4,8]. The structured interface is proposed to aid in interfacial delamination between the ganoine and bone layer and aid in dissipating energy from the bone to the ganoine [43].

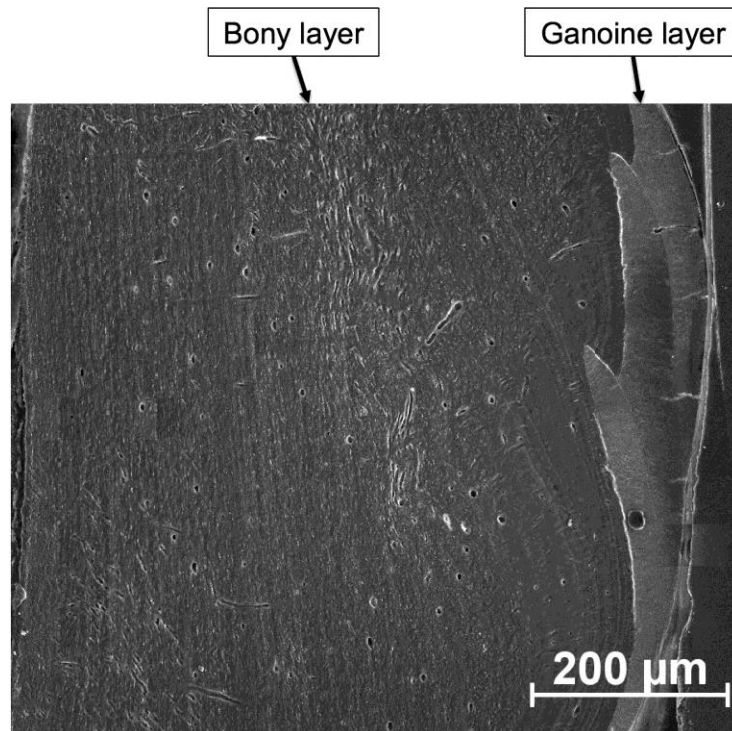


Figure 9: SEM image of the "sawtooth" structure ganoine bone interface [33]

3.2 Functional Grading of Material Properties

As seen in Figure 10, the brittle ganoine layer is highly mineralized, primary composed of HAp hexagonal nanorods (>95% biomineral content) with a varying thickness around 50μm with a total thickness of 800μm (Figure 1c) for the specimen tested by Allison et al. [33], Yang [34-35] and Chen [36] have reported adult Alligator gar fish scales thickness varying from approximately 500 to 4000μm.

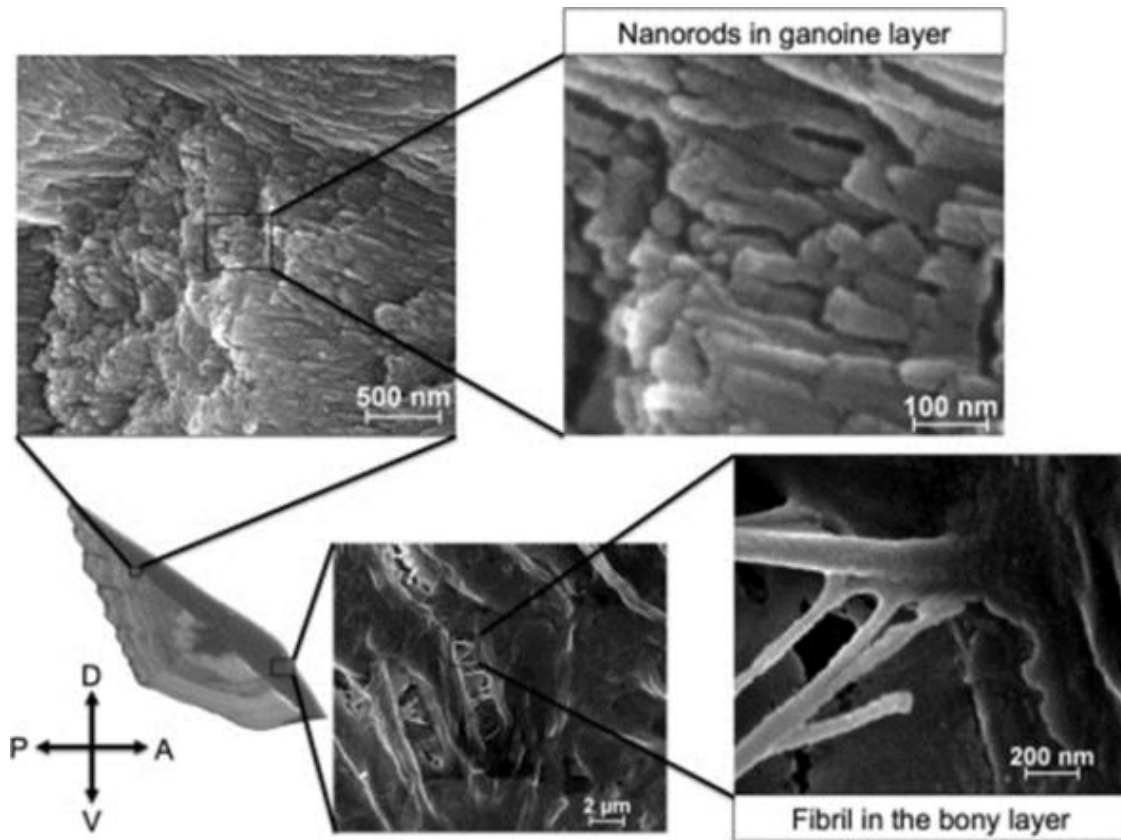


Figure 10: Hierarchical structure present in Alligator gar fish scale [33]

The HAp nanorods have a pseudoprismatic structure with ($\sim 45^\circ$ off axis alignment)[37]. The inner bone layer (750μm) is a combination of HAp platelets and collagen fiber bundles exhibiting viscoelastic material behavior [65].

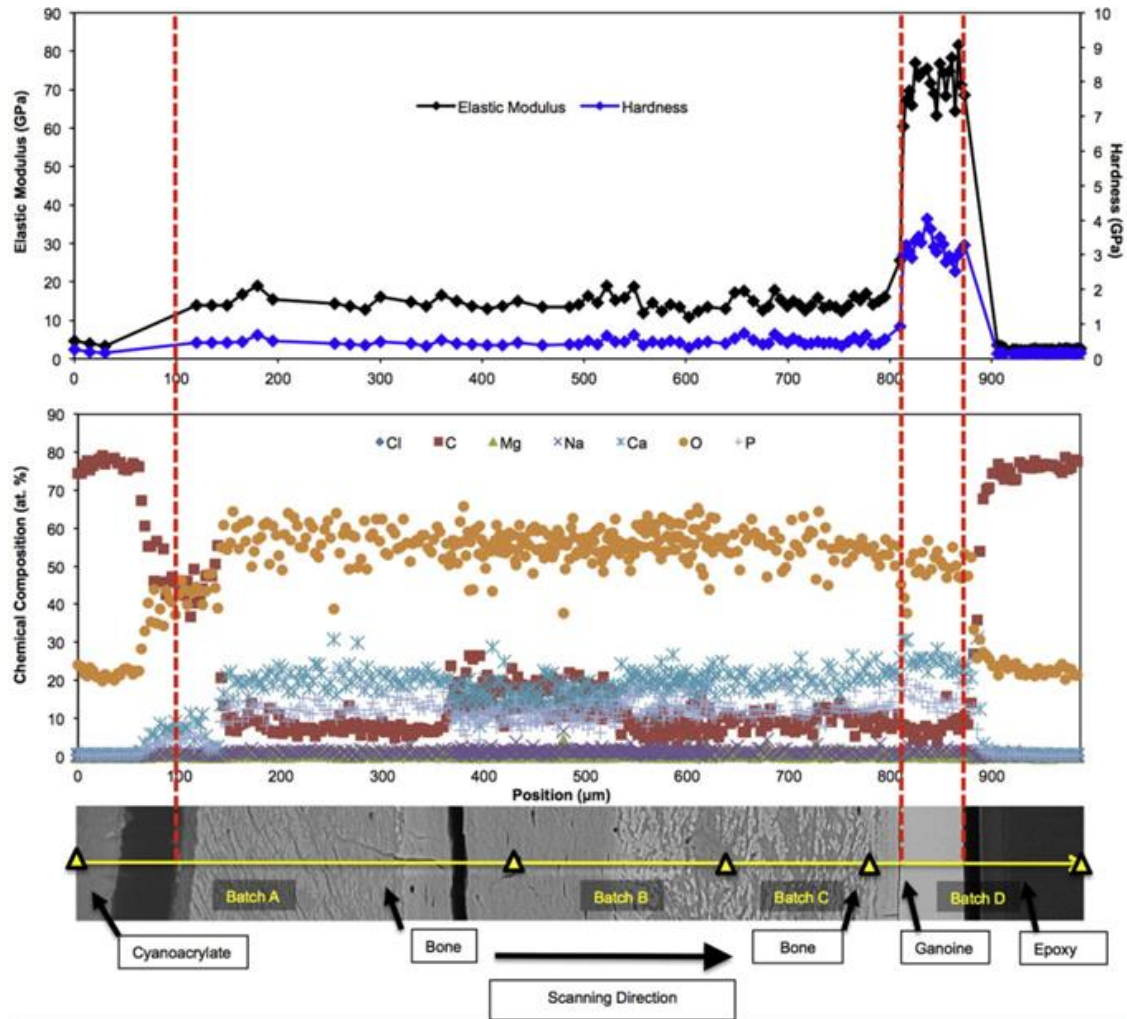


Figure 11: Material property variations in Alligator gar fish scale [33]

The layers are characterized by the decreasing mineralization progressing through the thickness [26]. Tai et al. [50] have shown the degree of mineralization effects on the mechanical response of bone tissue under nanoindentation and can be correlated to material properties at higher length scales. The material properties show a distinct higher order gradation of material properties that correlates with the composition variation as seen in Figure 11. The graded material properties shown in Figure 12 include elastic modulus, yield strength, and density.

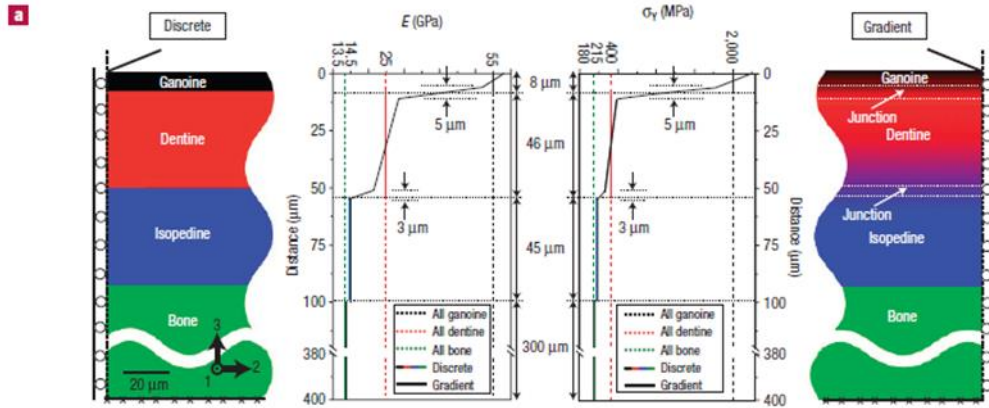


Figure 12: Functional grading of Gray bichir fish scale [31]

3.3 Delamination resistance

Delamination resistance has been shown in Alligator garfish scales at the ganoine-bone interface during microindentation testing [33]. This response is being studied for its energy dissipation properties as well as improved interface integrity for better engineering composites. This is of particular importance with bone biocomposite materials. Fracture has been reported to propagate perpendicular to the surface until it reaches this interface [33]. SEM images have shown the cracks then propagate along this interface (parallel to the ganoine surface) causing delamination (Figure 13).

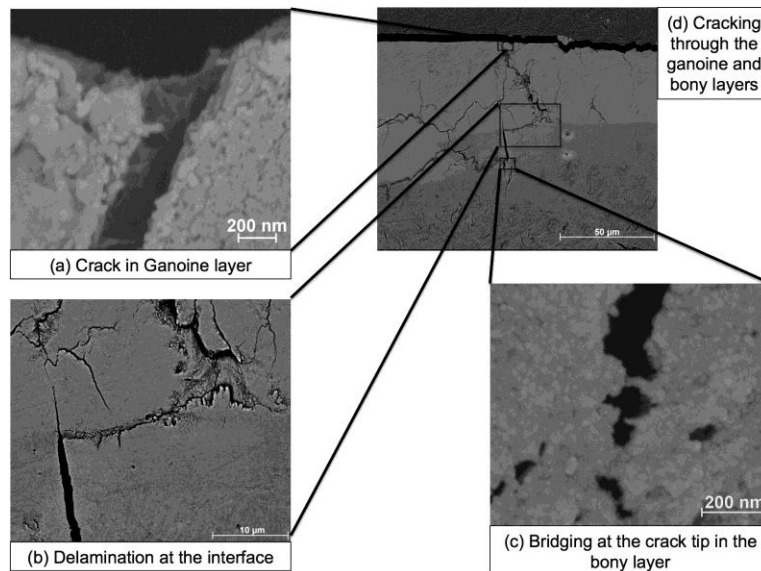


Figure 13: Delamination resistance of Alligator gar during indentation testing [33]

Collagen fibers, contain hydroxyproline amino acids which contain a side groups able to bond with the Ca^{+} surface ions (carboxylic acid and hydroxy groups) and the hydrogen atoms can also form hydrogen bonds with the phosphate group of HAp [79]. This phenomena has effects at all scales, from the nanoscale HAp interaction between collagen microfibrils and Hap nano-platelets to the mesoscale at the bone layer interfaces present in fish scale.

At the nanoscale, the flaw tolerance and fracture of bone-like hierarchal materials has been primarily investigated by Gao, Ji, Buehler, and Ritchie [18-23]. Studying the fracture mechanics of these materials has led to the development of a critical length scale at which the materials perform at near theoretical crystal strength. The critical length scale is a maximum value before flaws will start to effect material performance. Along with flaw tolerance, the nanometer scale of the constituents adds to the high work to fracture [18-19].

3.4 Hydration effects on mechanical behavior

Hydration and the electrochemical state of the surrounding environment have an effect on the mechanical behavior of collagen proteins, thus its effects have been of particular interest to biomaterials researchers. It also plays a significant role in the mechanical testing and performance of various biological structures. When dehydrated fish scales exhibit brittle failure as compared to the viscoelastic behavior of hydrated specimens, Figure 14.

The difference in biomaterials performance between hydrated and dehydrated test specimens has been attributed to the increase in direct chain to chain interaction in the presence of H_2O resulting in decreased slip between protein chains. Mechanical testing and MD simulations exhibited the significant difference between the “wet” ($E_{avg} = 0.6 \pm 0.2 \text{ GPa}$) and “dry” ($E_{avg} = 3.6 \text{ GPa}$) collagen fiber [78].

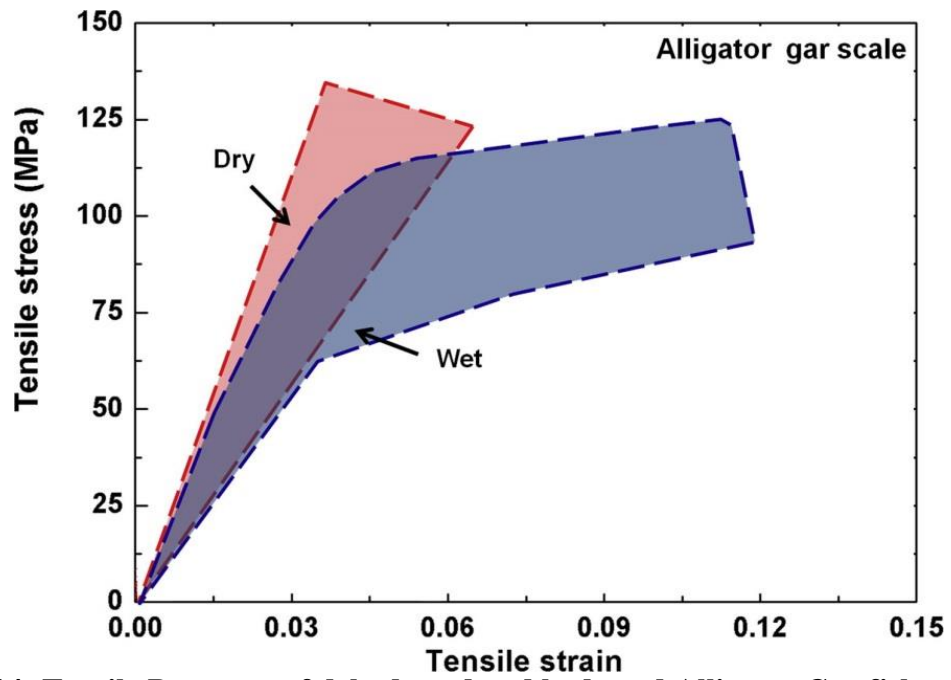


Figure 14: Tensile Response of dehydrated and hydrated Alligator Gar fish scales [34]

CHAPTER 4

METHODOLOGY

4.1 Generation of RVE Model

To be able to understand the fundamental effects that property and structural variations have on the intrinsic properties at the interface, FEM has been employed. A representative volume element (RVE) modeling approach for the ordered heterogeneous biomaterial systems has been used by several investigators [53-55,67] to capture the mechanical properties. The size or the length scale of the RVE for the Alligator gar was chosen as the typical though thickness of an adolescent fish scale in the ganoine covered region and the various layer thicknesses were determined from Scanning Electron Microscope (SEM) imagery [33]. The SEM image was discretized into one million voxels to cover a material volume of $800\mu\text{m} \times 800\mu\text{m} \times 800\mu\text{m}$ with a ganoine layer thickness of $72\mu\text{m}$, a sawtooth height of $48\mu\text{m}$, and a bone layer of $680\mu\text{m}$. With $100 \times 100 \times 100$ voxels, one-million element cube with a 8-micron resolution, was created using an in-house Matlab preprocessor.

For the RVE, the ganoine is assumed to cover the entire surface, all layers are constant thickness, and the sawtooth pattern has approximately $160\mu\text{m}$ periodic domain. The in-house Matlab preprocessor was employed to generate the fish scale microstructure. The layer thickness, material property grading, and interfacial geometry for each of the one million elements were designated. All material layers were modeled as elastic-perfectly plastic. Simulations were run using ABAQUS[®] finite element software.

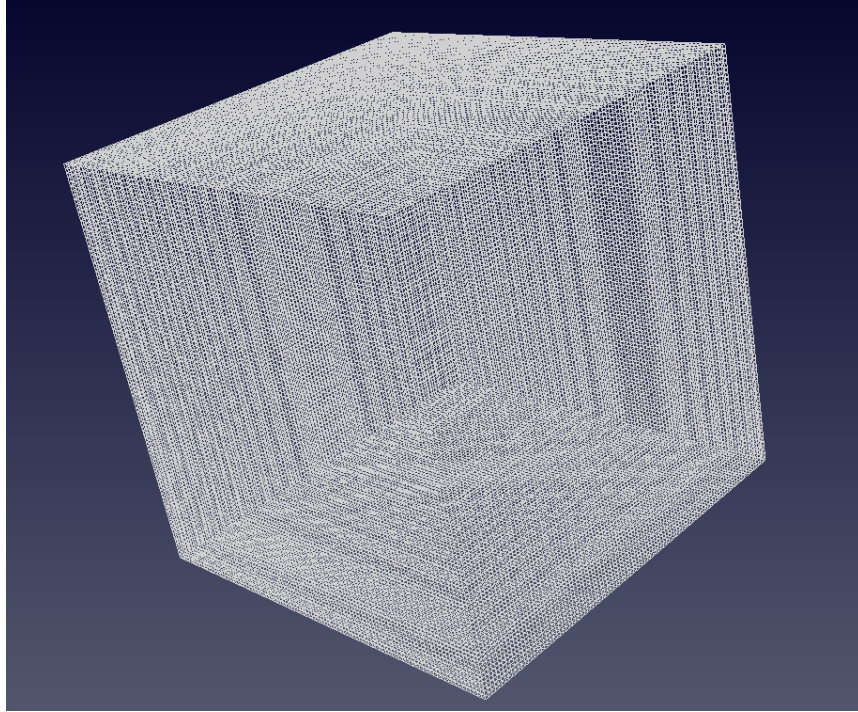


Figure 15: One million element RVE mesh

4.2 Representative volume element

The finite element analysis (FEA) is based on a microscopic representative volume element (RVE) of the fish scale with an overall thickness of 800 micron. The FEA RVE had one million uniform 8-micron size cubical 8-node elements. The geometrically nonlinear sawtooth features are explicitly modeled. To determine the effective elastic properties for the fish scale, the material response was initially assumed to be elastic. However, in the energy dissipation analysis, the material response was modeled with a simplistic elastic- perfectly plastic behavior. For a qualitative understanding, the RVE analysis assumed an average yield stress for all layers. The modeling and simulation was performed using commercially available general purpose three dimensional ABAQUS[®] finite element (FE) software along with in-house Matlab preprocessors, and computing resources from the Mississippi Center for Supercomputing Research. High-resolution finite element modeling was the basis for developing a functionally graded and

geometrically interlocked model to describe the response of fish scale to external stimuli. Table 1 shows material property variations used for the RVE model generation.

Table 1: RVE layers and property grading for Alligator gar fish scale

Layer	Thickness (μm)	Elements/layers	Elastic Modulus (GPa)	Yield Strength (GPa)	Possion's ratio
Ganoine	72	9	60-82	1.05	0.28 [34]
Interface	48	6	20-60	0.18-1.05	0.30 [94]
Bone	680	85	13-20	0.18	0.30 [94]

All layer thicknesses were determined by SEM image analysis from experimental characterization performed by Allison et al. [33]. The structured was idealized for initial investigations into the effects material property grading and structured interface on stress distribution, particularly at the interface, and elastic energy. Lastly, an elastic – perfectly plastic material model was employed to determine the energy dissipation mechanisms for average strain condition large enough to induce plastic yielding, but below ultimate failure strain.

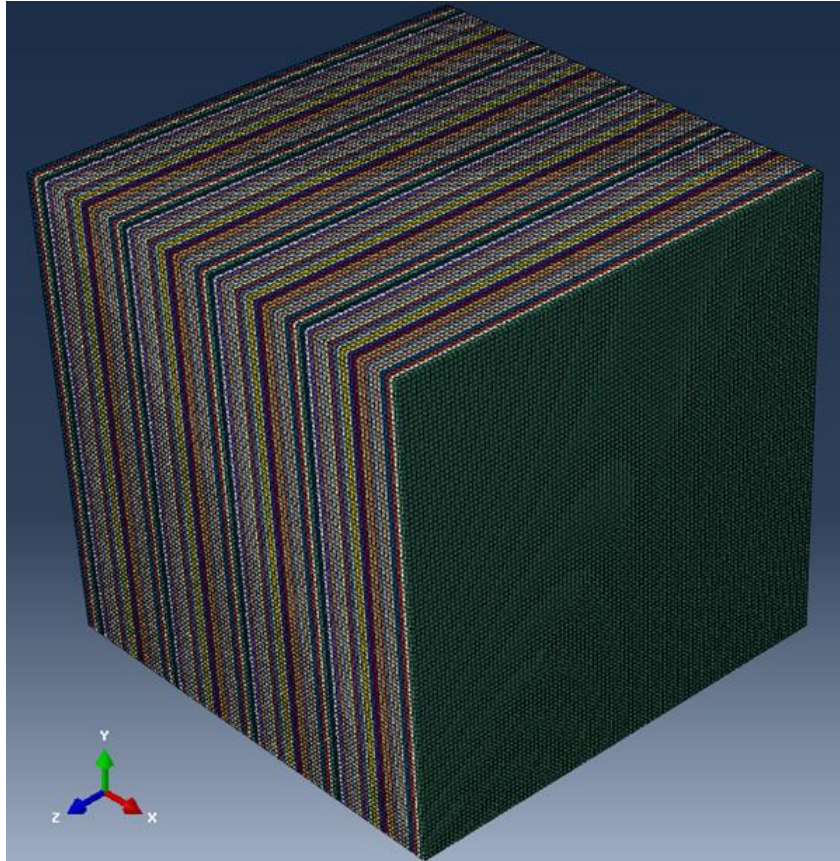


Figure 16: ABAQUS® RVE of functionally graded material model

4.3 Functional Gradation for RVE simulations

To grade the elastic modulus through the thickness a power law function was used to interpolate between layer end points. A power law was chosen to allow for empirical fit of indentation data for increased accuracy of property variations. The material grading function produces a smooth curve so the resulting moduli are discretized into materials with similar properties. Initial results have been obtained using linear gradation of material properties as proposed by Bruet et al. [31].

Equation 1 returns a value between 0 and 1 then multiplies the layers modulus difference, yield strength, and density to return a graded property value. For initial simulations $a=1$ to produce a linear gradation of desired properties.

$$\phi_n(x) = \left(\frac{x_2 - x_i}{x_2 - x_1} \right)^\alpha \quad (1)$$

$$E(x) = \Delta E \phi_n(x) + E_n \quad (2)$$

$$\sigma_y(x) = \Delta \sigma_y \phi_n(x) + \sigma_{y_n} \quad (3)$$

$\phi_n(x)$ is relative grading of the material property for each layer and returns a value between 0 and 1 depending on depth within the layer, x_i . ΔE and $\Delta \sigma_y$ are the change in elastic modulus and yield strength for a given layer; E_n and σ_{y_n} are elastic modulus and yield strength at the inner boundary for each layer. Equations 2 and 3 determine the elastic modulus and yield strength for a given element. The material properties are assumed to be consistent in the z direction. Figure 17 shows the material property grading through the thickness of the fish scale. The stiff, high strength ganoine layer on the left and the compliant bone layer on the right in Figures 17 and 18.

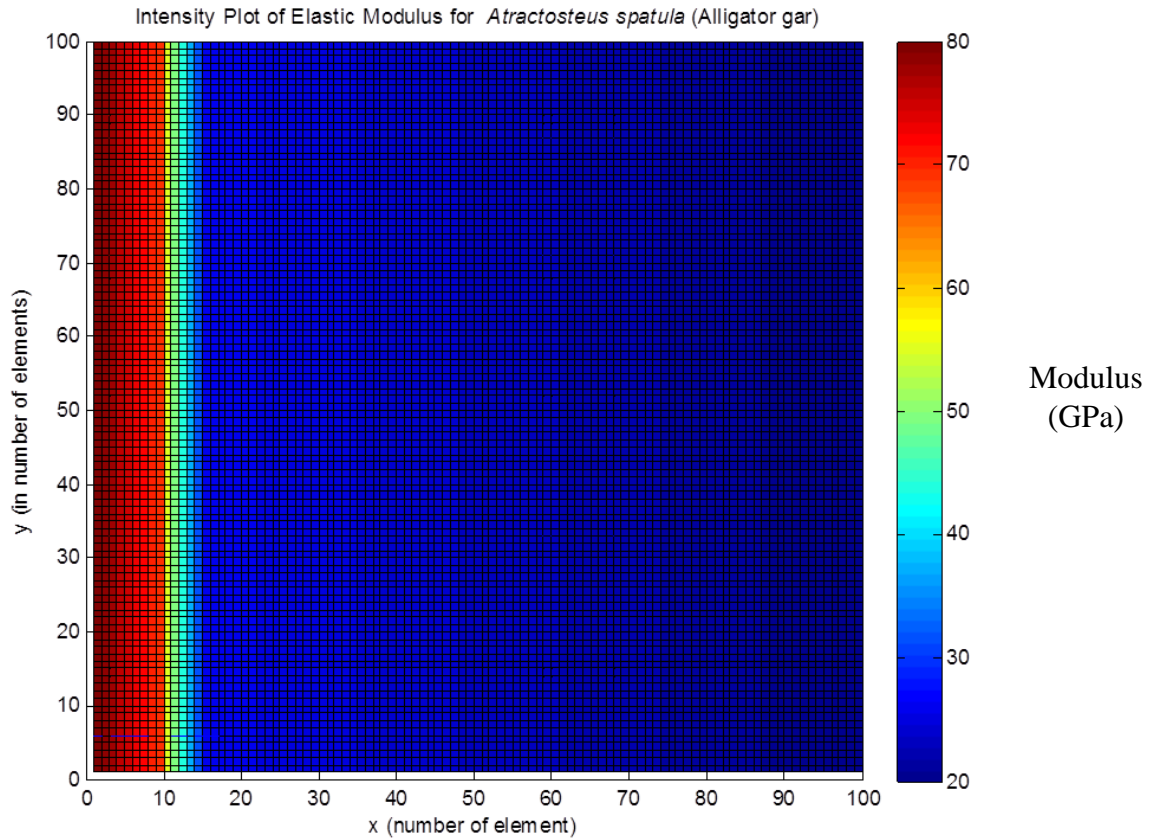


Figure 17: RVE functional grading intensity plot of elastic modulus for representative layer

4.4 Geometrically interlocked interface

Alligator gar fish scale exhibits a geometrically interlocked interface between the stiff ganoine outer layer and the compliant bone inner layer. The interface exhibits a distinct periodic sawtooth structure with the ganoine layer intruding into the interfacial region of the fish scale. For the RVE it was assumed that the sawtooth structure was periodic with a spacing of $160\mu\text{m}$ and peak height $48\mu\text{m}$. The influence of the sawtooth shape is also investigated to determine the effects on stress distribution at the interface. The sawtooth configuration has been generated using a power law to allow for investigation into the effects of tooth geometry on mechanical performance.

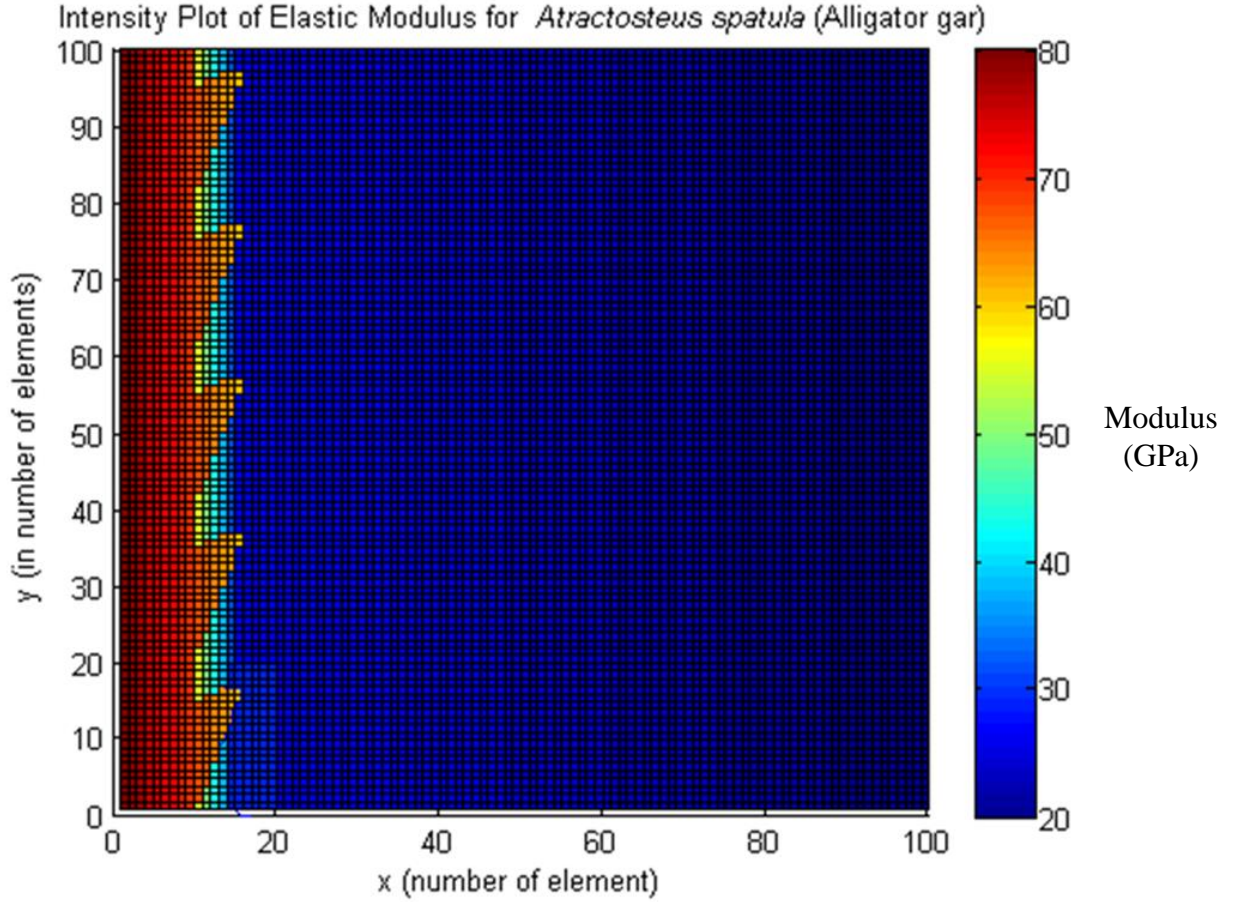


Figure 18: RVE functional grading intensity plot of elastic modulus for sawtooth intrusion

4.5 Boundary Conditions

In this study, both extrinsic and intrinsic mechanical properties were determined by using both periodic (PBC) and kinematic boundary conditions (KBC). Since the RVE size can significantly alter the results, it is important to evaluate the influence of BCs on the FEM results for the chosen size. To make sure that the 800 micron RVE size is realistic in the determination of effective elastic moduli and the results are not affected by the boundary condition assumptions, the RVE responses to various loading conditions with either PBC or KBC are compared. In addition, the detailed post processing of ABAQUS® results using ParaView visualization software, such as the PYTHON guided the analysis to evaluate the effects of

various geometrical features and the functional gradation of elastic properties on the redistribution of stress and strain energy for efficient energy dissipation.

Displacements were applied in all three-principle directions to determine RVE anisotropy due to geometric configuration and property variations. The prescribed displacements were applied to the appropriate surfaces and the others left free for the KBC.

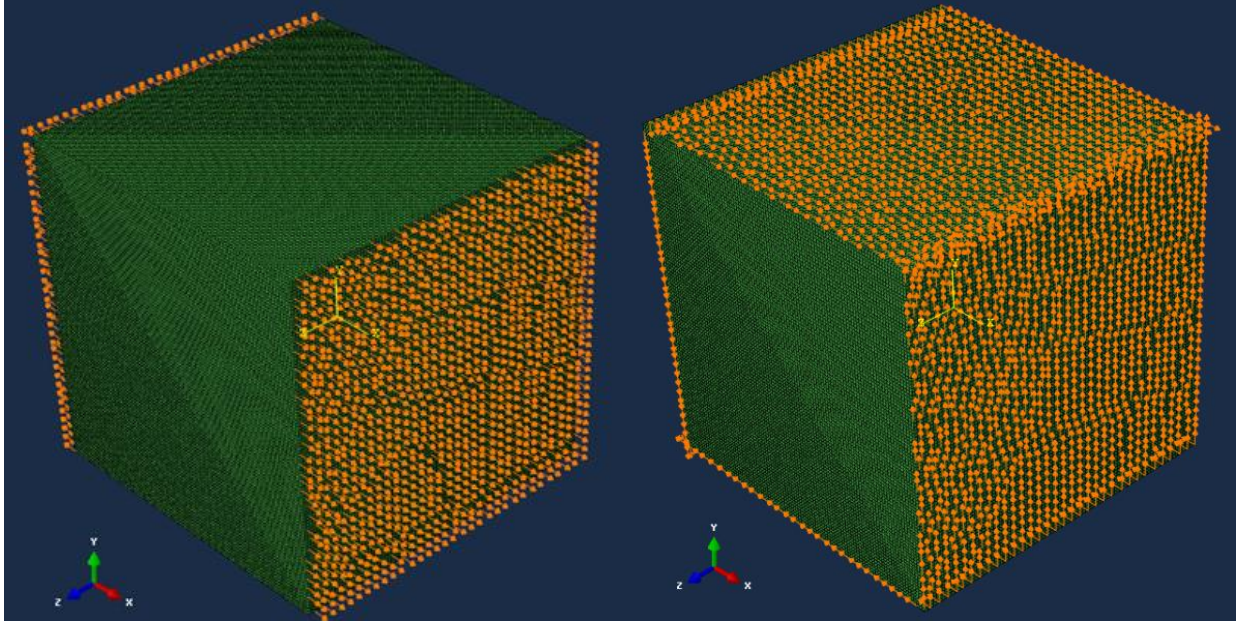


Figure 19: Kinematic boundary conditions: uniaxial (left) and shear (right) displacement conditions

The periodic boundary condition allows for analysis of the RVE in a continuous material domain (lateral surface at infinity) and enables comparison with the finite RVE response with kinematic boundary conditions. For all simulations displacement boundary conditions are employed to ensure an average RVE strain and combined with an energy homogenization approach to determine the RVE elastic modulus. Periodic Boundary conditions are enforced using *EQUATION keyword [94]. All simulations were run with 0.1% average strain applied.

CHAPTER 5

FINITE ELEMENT ANALYSIS RESULTS

5.1 ABAQUS® Simulation Results

In this section, the RVE results were obtained for displacement boundary conditions only. Since the RVE is truly an anisotropic heterogeneous material, it is non-trivial to achieve a perfect uniaxial stress distribution through the thickness direction, as a first order approximation, both top and bottom surfaces were uniformly pulled under a static loading condition without any rate effects. Unfortunately, this uniaxial pulling generates in plane shear (xy) and normal stresses in the transverse directions. The shear stresses in the xz and yz planes were found to be almost negligible. Since the volume associated with these (ganoine – bone interface) regions are relatively very small compared to the total volume of the RVE, the elastic properties were estimated through the homogenization approach. The high resolution computational results for an RVE with one-million elements provided insights into the effects of varying gradation of material properties along the thickness as well as the interlocking structural features on effective macro-level material properties, stress localization, and energy dissipation. An energy homogenization approach (equations 4-7) was used to determine the effective elastic modulus for each of the given loading and boundary conditions.

$$U = \frac{1}{2} \sigma_{ij}^{avg} \varepsilon_{jk}^{avg} V_{RVE} \quad (4)$$

$$\sigma_{ij}^{avg} = E_{ik} \cdot \varepsilon_{kj}^{avg} \quad (5)$$

$$U = \frac{1}{2} E_{ij} (\varepsilon_{jk}^{avg})^2 V_{RVE} \quad (6)$$

$$E_{ij} = \frac{2U}{(\varepsilon_{jk}^{avg})^2 V_{RVE}} \quad (7)$$

U is the strain energy for a linear elastic material, σ_{ij}^{avg} is the average RVE stress, ε_{jk}^{avg} is the average RVE strain, V_{RVE} is the RVE, and E_{ij} is the effective elastic modulus for the RVE. The effective properties determined for both PBC and KBC when applying a prescribed displacement in principal and shear directions are given in Table 2. The results show good agreement between PBC and KBC. Since the elastic properties for individual elements are assumed as isotropic and the functional grading of the material is assumed only in the thickness direction, the overall response of the 800 micron thick fish scale is very close to orthotropic elastic behavior (Table 2 and 3). Simulations show an increased effective modulus (E_{22}) the transverse direction (~23.5 GPa) and more compliant response when loaded normal to the functional grading. Both models were compared with the inverse rule of mixtures for the x-direction (thickness direction) and the conventional rule of mixtures for the y (or z) -direction due the material orientations being consistent with the theoretical formulations for the respective equations.

It is important to note that the geometrical features in the y and z directions are different due to the presence of the saw tooth structure. However, the volume percentage of the idealized sawtooth domain compared to the total volume is not large enough to show any significant difference between the estimated E_{22} and E_{33} . An independent parametric study needs to be performed to determine the effects of structural variations and interface transition zone thickness. To investigate this aspect, simulations were performed with a RVE that did not include the sawtooth feature; however, the functional gradation was kept the same as in the RVE with

sawtooth features (Table 3). A comparison between the moduli for the two cases: 1) with sawtooth, and 2) without sawtooth, further convinces that the effective elastic moduli were not significantly influenced by the saw tooth structures.

Table 2: Effective macroscale properties for Alligator gar fish scale RVE - Sawtooth

100x100x100 voxel model	PBC	KBC	
Modulus	Effective modulus (GPa)	Effective modulus (GPa)	Rule of mixtures (GPa)
E11	18.23	18.29	18.07
E22	23.45	23.46	23.56
E12	6.97	6.97	6.95

Table 3: Effective macroscale properties for Alligator gar fish scale RVE - Planar

100x100x100 voxel model	PBC	KBC	
Modulus	Effective modulus (GPa)	Effective modulus (GPa)	Rule of mixtures (GPa)
E11	18.11	18.20	18.03
E22	23.04	23.00	23.00
E12	6.97	6.96	6.94

5.3 Stress distribution due to structured interface and functional graded material properties

Figure 20 shows the contour plots of the three normal stresses and three shear stresses due to uniform displacement applied to the “yz” faces ($x=0$ and $x=800$ microns) in tension. Due to the presence of sawtooth structure and the steep spatial gradients of elastic modulus around the interface, the stress response becomes locally anisotropic. The maximum tensile stresses are around 3 MPa in the sawtooth region. However, the transverse stresses (σ_{yy}/σ_{zz} or σ_{22}/σ_{33}) become compressive in this region due to high modulus (Figure 20) and created local periodic stress distribution in the 48-micron thick /bone interface indicates redistribution of stresses in a complex manner through stress reductions in the bone layer deeper into the fish scale thickness. Also evident is the significantly lower stress experienced in the ganoine layer due to the bone layer being largely responsible for elastic stress absorption. The sawtooth pattern appears to create tensile stress in the transverse directions, but the stress in the interfacial region is lower than the surrounding material potentially leading to increased interfacial integrity.

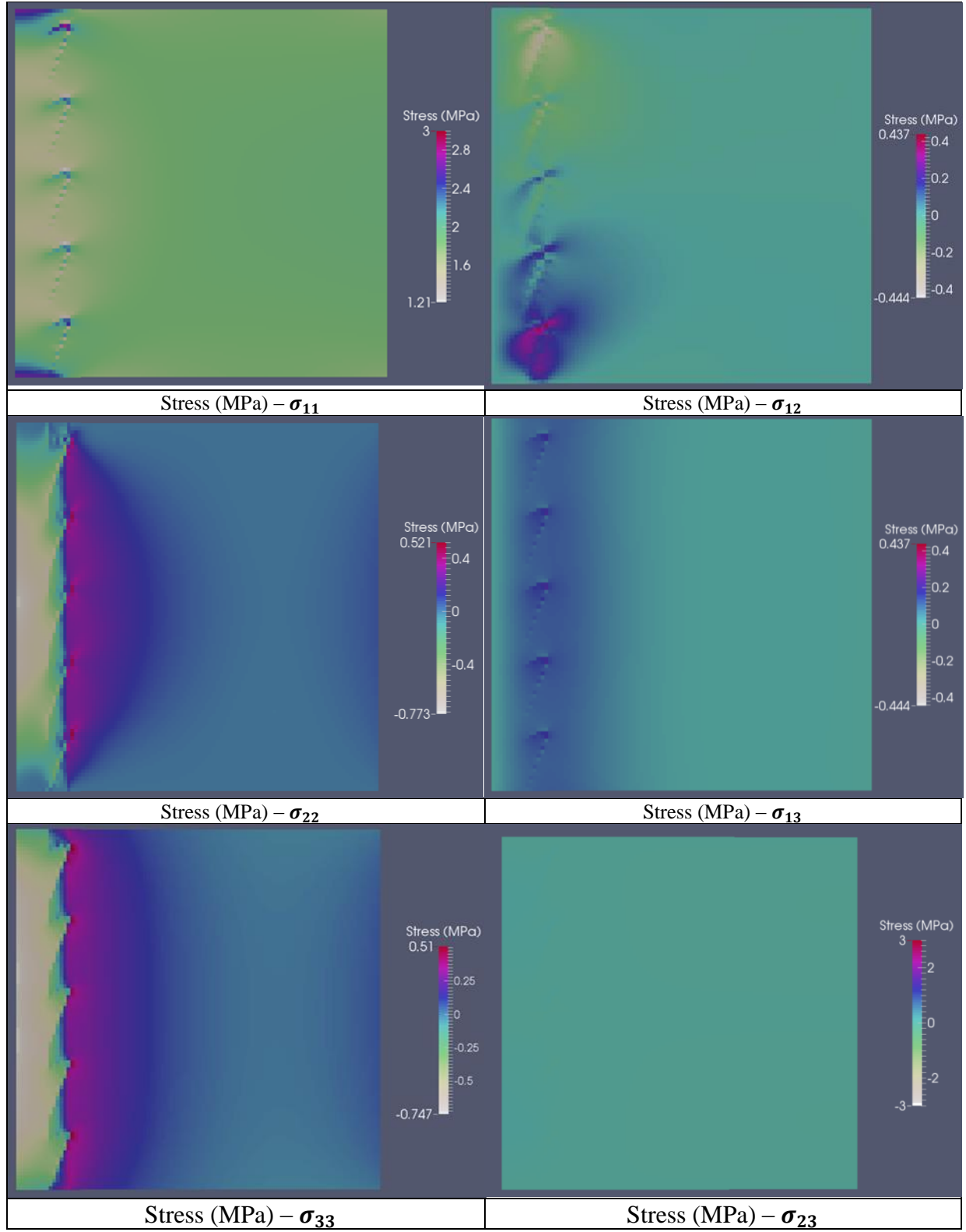


Figure 20: RVE stress distribution under uniaxial displace condition with the sawtooth(u₁₁)

To determine the effect of the structured interface the stresses for a u_{11} displacement condition for a representative section were normalized by the RVE average stress. The ganoine layer shows a sinusoidal-like normalized stress distribution ranging between 81% and 94% (Figure 21).

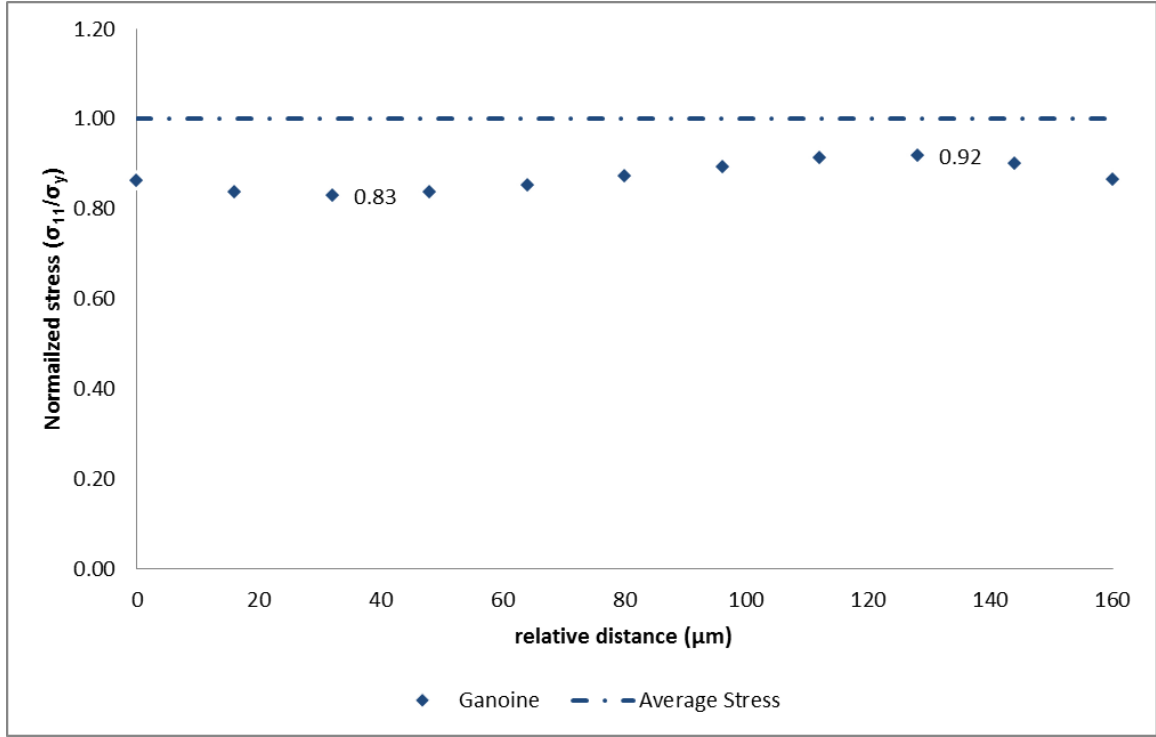


Figure 21: Normalized stress (σ_{11}/σ_y) in the ganoine for Alligator gar under uniaxial loading conditions

The interface shows a normalized stress level in the ganoine sawtooth at 23% above the average stress and a 20% below the average RVE stress. The interfacial layer shows stress concentrating at the tip of the ganoine intrusion resulting in a reduced stress in the local interface material (Figure 22). The sawtooth structure providing a reduced stress in the interfacial layer the mechanical integrity will be maintained for larger effective strain conditions allowing for a more robust interface.

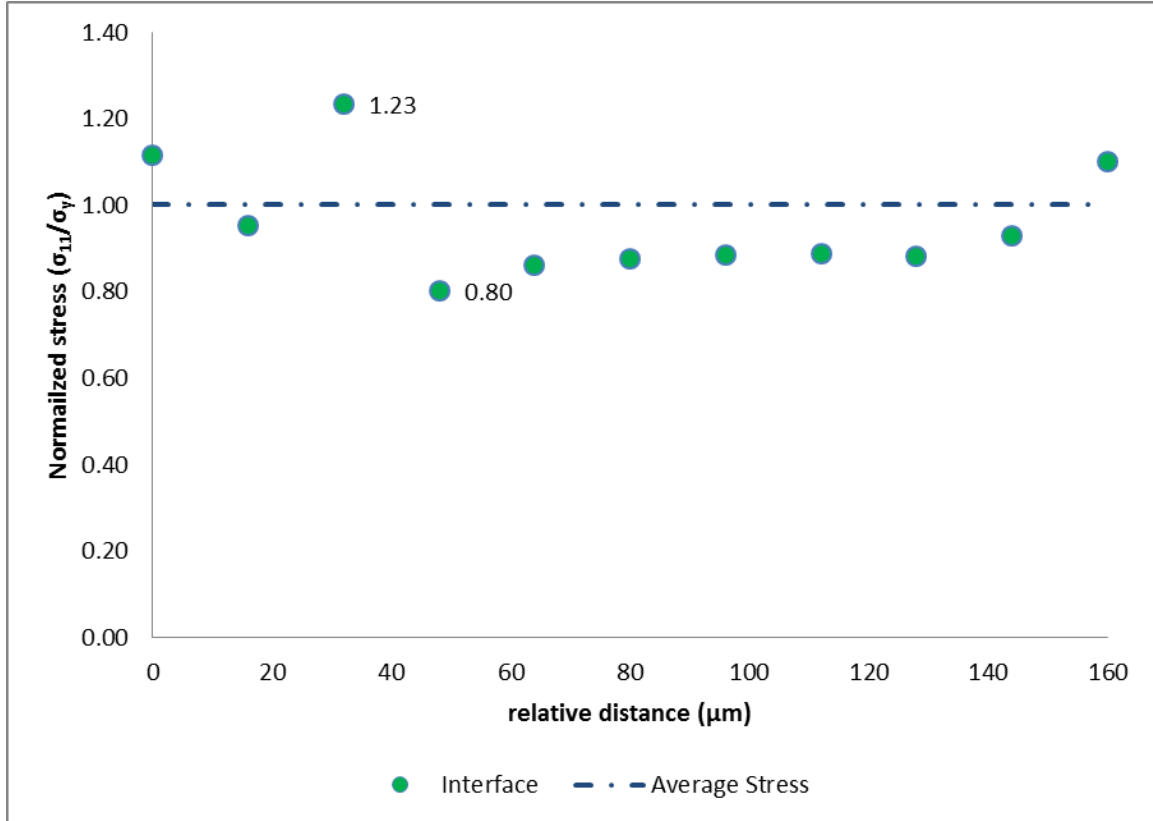


Figure 22: Normalized stress (σ_{11}/σ_y) in the ganoine for Alligator gar under uniaxial loading conditions

Figure 23 is the RVE without the sawtooth structured interface for u_{11} displacement condition. Of note is the stress state near the interfacial region. Comparatively with the saw-tooth plot the functionally graded model shows stress concentrations at the interface compared to the diffuse stress state exhibited around the saw-tooth. Given the importance of interfacial integrity to composite materials, the structured interface appears to benefit the RVE mechanical response by dissipating the stress into the bone layer where delamination is not going to occur. In addition, shear stress develops in the (u_{13}) direction whereas the shear is redistributed along to the stronger ganoine side of the saw-tooth interface.

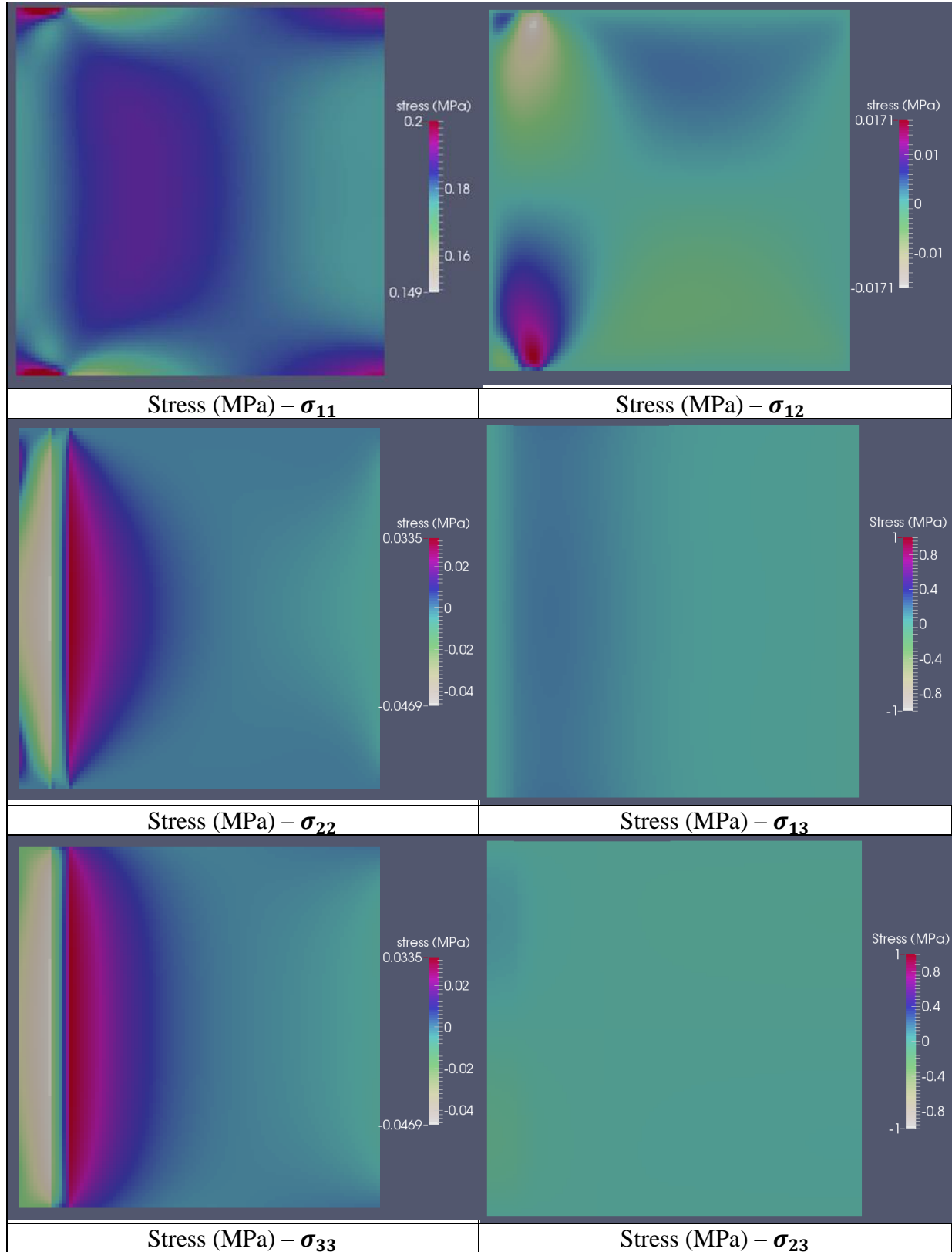


Figure 23: RVE stress distribution under uniaxial displacement condition without the sawtooth (u_{11})

Stresses were extracted from the ABAQUS® ODB file for each integration point and averaged to allow for analysis of the stress distribution within the RVE. Under transverse displacement condition the stress is being redistributed by the ganoine layer leading to the bone layer having a much low stress state. This can be attributed to the significantly higher Young's modulus for the ganoine layer. The stress transverse to the loading direction shows an uneven stress distribution at the interface with stress localizing the sawtooth structures and significant decrease in stress across the interface. For more details see plots for the transverse displacement conditions (u_{22} and u_{33}) located in the Appendix B.

5.3 Structured interface under shear loading conditions

FEA simulations have shown the ganoine intrusions to aid in shear stress reduction at the interface. Stress concentrations develop at the tip of the sawtooth structure and there is an immediate stress reduction in the interfacial region of the bone layer. Figure 24 shows the RVE response to positive and negative shear loading conditions. The stress intensity plots show the characteristic stress bands developed due to the sawtooth structure at the ganoine-bone interface with reduced stress in transition region. Figure 25 shows the stress concentrating in the ganoine sawtooth and reduced stress in the adjacent interface region.

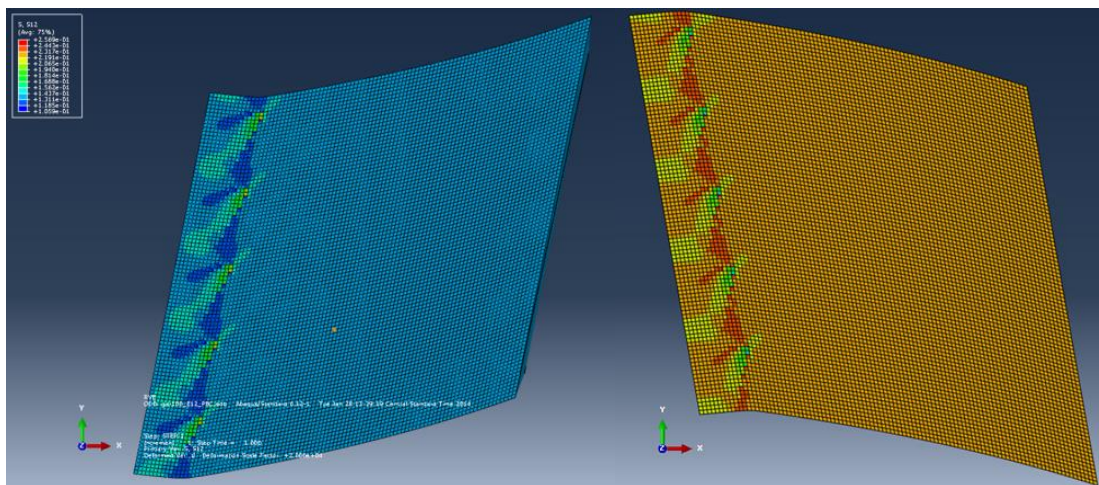


Figure 24: Shear stress response of Alligator gar fish scale

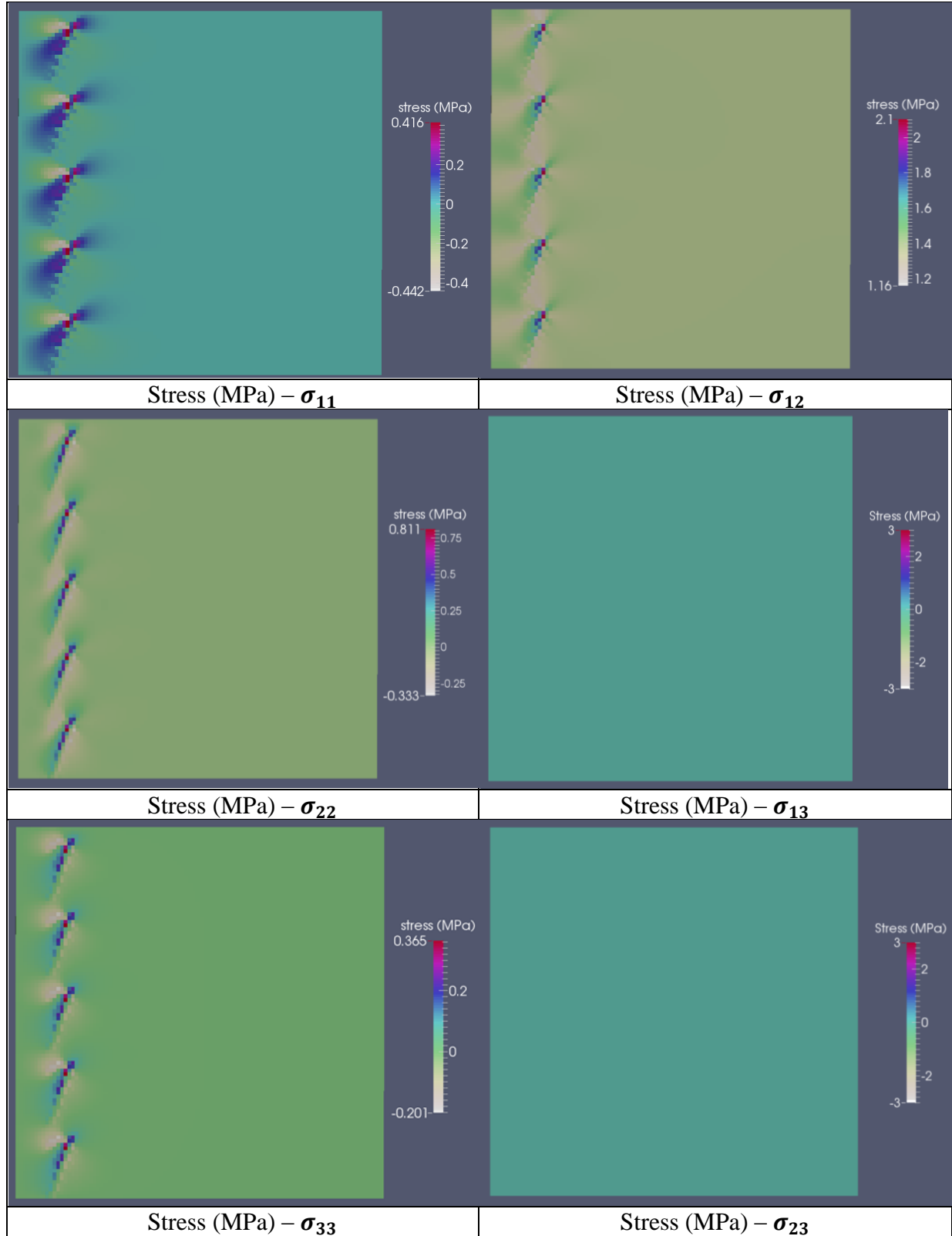


Figure 25: RVE stress distribution under shear displacement condition (u_{12})

Results have shown the normalized stress to reach a maximum of 1.32 on the sawtooth and reduce to 0.87 in the interface region (Figure 26). The stress in the interface region is concentrating in the stronger ganoine intrusion leaving a reduced stress in bone interface material. This stress reduction is proposed to improve interfacial strength and structural integrity under shear strain conditions. Further analysis will be performed to determine any variations in localized response to the applied displacement conditions.

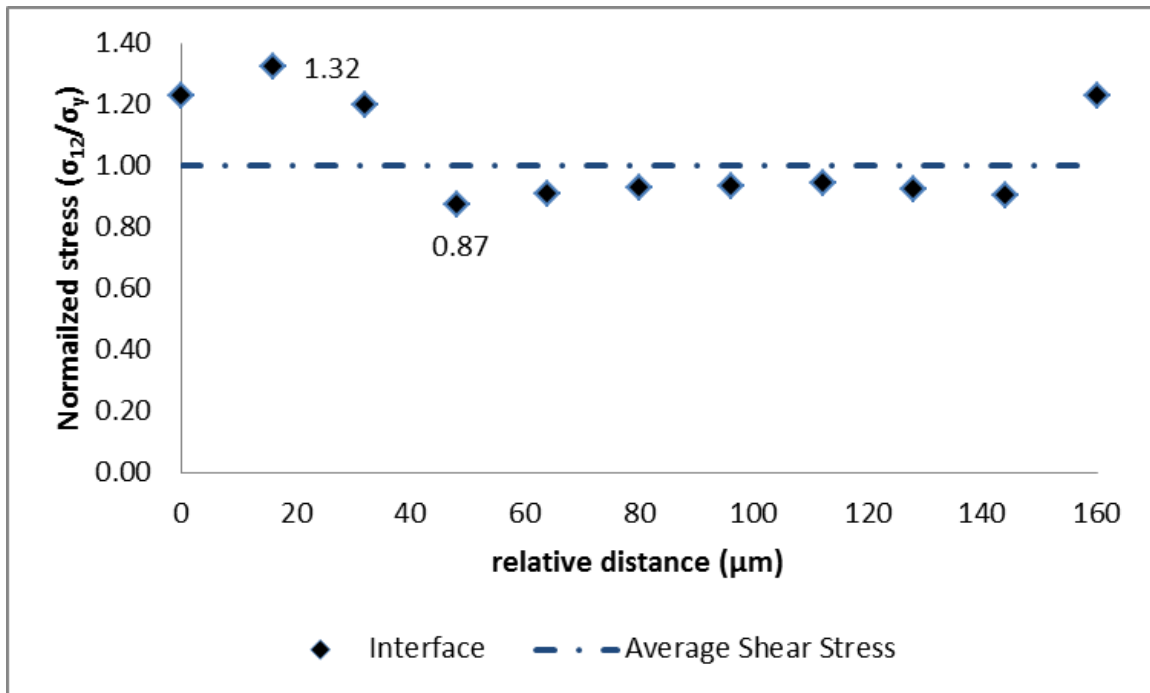


Figure 26: Normalized stress (σ_{12}/σ_y) at the interface for sawtooth interlocked model

The reduction in normalized stress present in the interfacial region could potentially aid in interface integrity. The stress concentrates in the high strength ganoine material present in the sawtooth intrusions and provides a distinct lowering in the interfacial region below the average RVE shear stress.

5.4 Elastic Energy Dissipation

The elastic energy density for the RVE was analyzed to determine the effect of the structured interface and functional gradation of material properties. The energy density is representative of the energy per unit volume. As can be seen in the following figures the bone layer plays a significant role in energy absorption and allows the ganoine layer to stay in a low stress state when loaded in the through thickness direction. U is the elastic energy.

$$U = \frac{1}{2} \sigma_{ij} \varepsilon_{ij} \quad (8)$$

Under u_{11} displacement condition, the ganoine layer is in a lower energy state would allow for significantly more deformation prior to failure. Table 4 is the strain energy density for each layer at the other most surfaces. The bone layer shows significantly more strain energy for the u_{11} and u_{12} displacement boundary conditions. With the strain energy in the ganoine layer being nearly zero for shear displacement.

Table 4: Strain energy density for the ganoine and bone layers

Energy Density ($\mu\text{J}/\text{mm}^3$)		
Boundary Condition	Ganoine	Bone
u_{11}	30	157
u_{22}	431	53
u_{33}	410	65
u_{12}	0.3	194

To aid in analyzing the energy distribution the strain energy density by element was visualized using a PYTHON postprocessor for input into ParaView visualization software. For more details on postprocessor development see Appendix A. The results show a non-uniform distribution of strain energy density. The energy variations correlate the decreasing modulus. In the case of the u_{11} displacement condition there is an inverse correlation with the strain energy

density increasing from $30 \mu\text{J}/\text{mm}^3$ to $157 \mu\text{J}/\text{mm}^3$ in the bone layer. For both of the loading conditions transverse to the property grading there is a direct correlation to the elastic modulus. For the u_{22} and u_{33} displacements the ganoine layer has strain energy densities of 431 and $410 \mu\text{J}/\text{mm}^3$ with a gradual decrease to 53 and $65 \mu\text{J}/\text{mm}^3$ respectively.

The distinct response to a given loading condition would indicate a preferential gradation of material properties for u_{11} and shear displacement conditions. Given the typical load applied will be consistent with the displacements the potential for evolved protective properties should be further investigated. Indications are that the development of these protective fish scales has provided specific advantageous response to compressive loading conditions from the ganoine towards the bone layer.

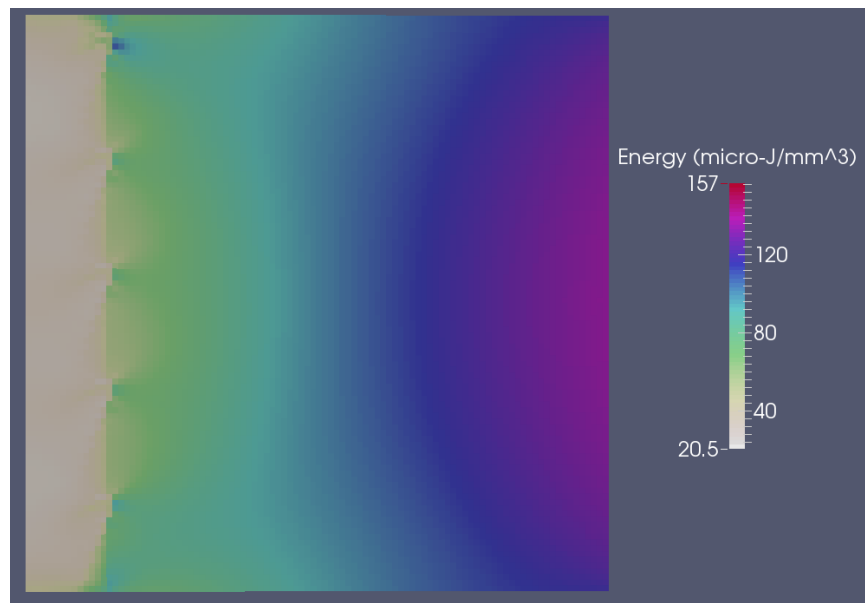


Figure 27: Strain energy density for u_{11} displacement condition

For the prescribed u_{22} displacement condition the ganoine layer displays a significantly higher energy state. This can be attributed to the higher elastic modulus in the ganoine layer. Due to the low stress and energy state under u_{11} and u_{12} displacements compared to the transverse loading the Alligator gar fish scale appears to have a preferential material layup to resist compressive force consistent with the predatory loading experienced in the natural environment.

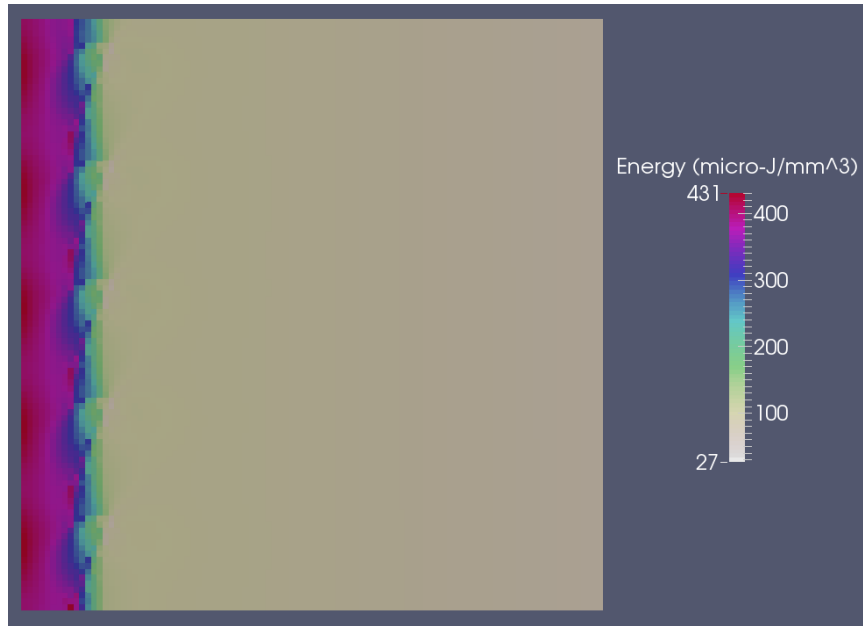


Figure 28: Strain energy density for u_{22} displacement condition

Of particular interest is the RVE's response to shear loading condition due to the dominance of shear failure in ductile materials. Under shear loading the bone layer displays significantly more deformation and energy absorption. The most compliant region of bone layer dissipates 7.2 times more strain energy than the ganoine layer. As seen in the u_{11} , the bone layers energy dissipation leaves the ganoine layer capable of absorbing significantly more energy prior to failure.

Similar to the u_{22} boundary condition, the u_{33} displacement simulations results show the strain energy density concentrating in the ganoine layer and a low energy state in the bone layer. The ganoine layer, with $410 \mu\text{J}/\text{mm}^3$ has 6 times the strain energy density with a progressive decrease to $0.65 \mu\text{J}/\text{mm}^3$. The energy distribution between layers is dependent on boundary conditions, which also supports the preferential material layup for specific loading conditions such as predation attacks by other fish trying to penetrate the exterior scales.

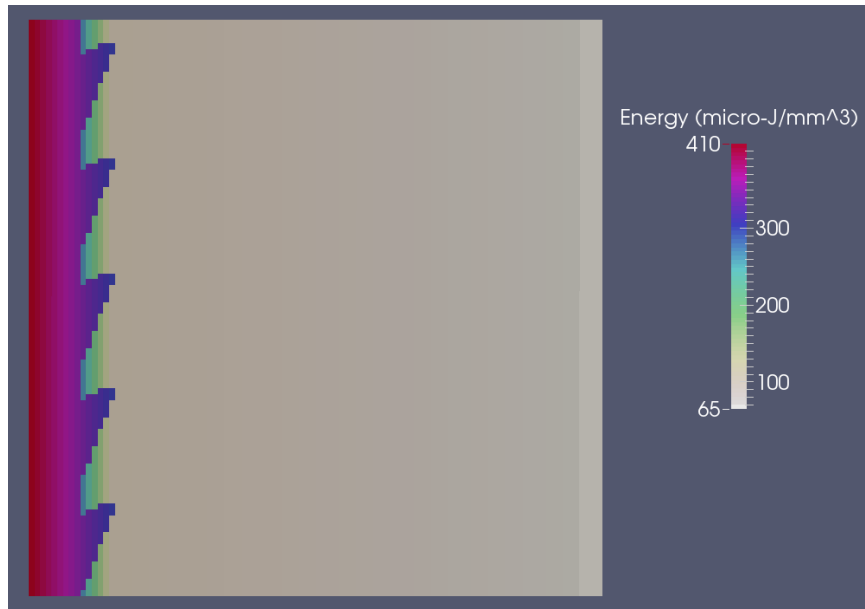


Figure 29: Strain energy density for u_{33} displacement condition

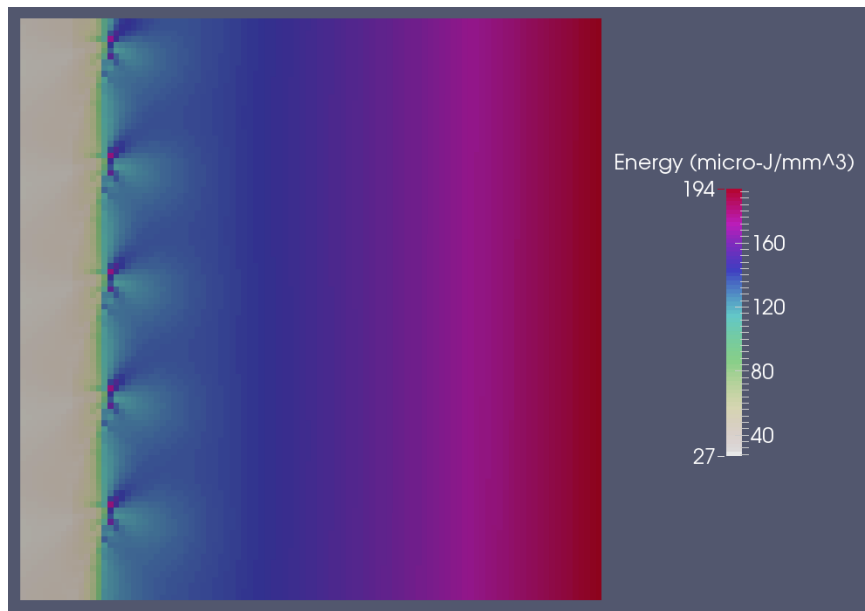


Figure 30: Strain energy density for u_{12} displacement condition

5.4 Elastic - Perfectly Plastic Compression simulations

Multistep compression simulations were run on a single sawtooth model to characterize the localized stress distribution across the ganoine-bone interface. Figure 31 shows the stress-strain curves for 4 elements located near the tip of the sawtooth during the elastic portion of the

loading. The tip of the sawtooth shows to have increased stress values 34% above the RVE effective stress, with a normalized stress of 1.34. Immediately across the interface the stress is significantly reduced down to below the effective stress reaching a minimum value of 0.81 for the normalized stress. Simulation results seem to indicate stress dissipation is occurring through stress localization in the sawtooth intrusion allowing for a more diffuse stress state in and around the interface.

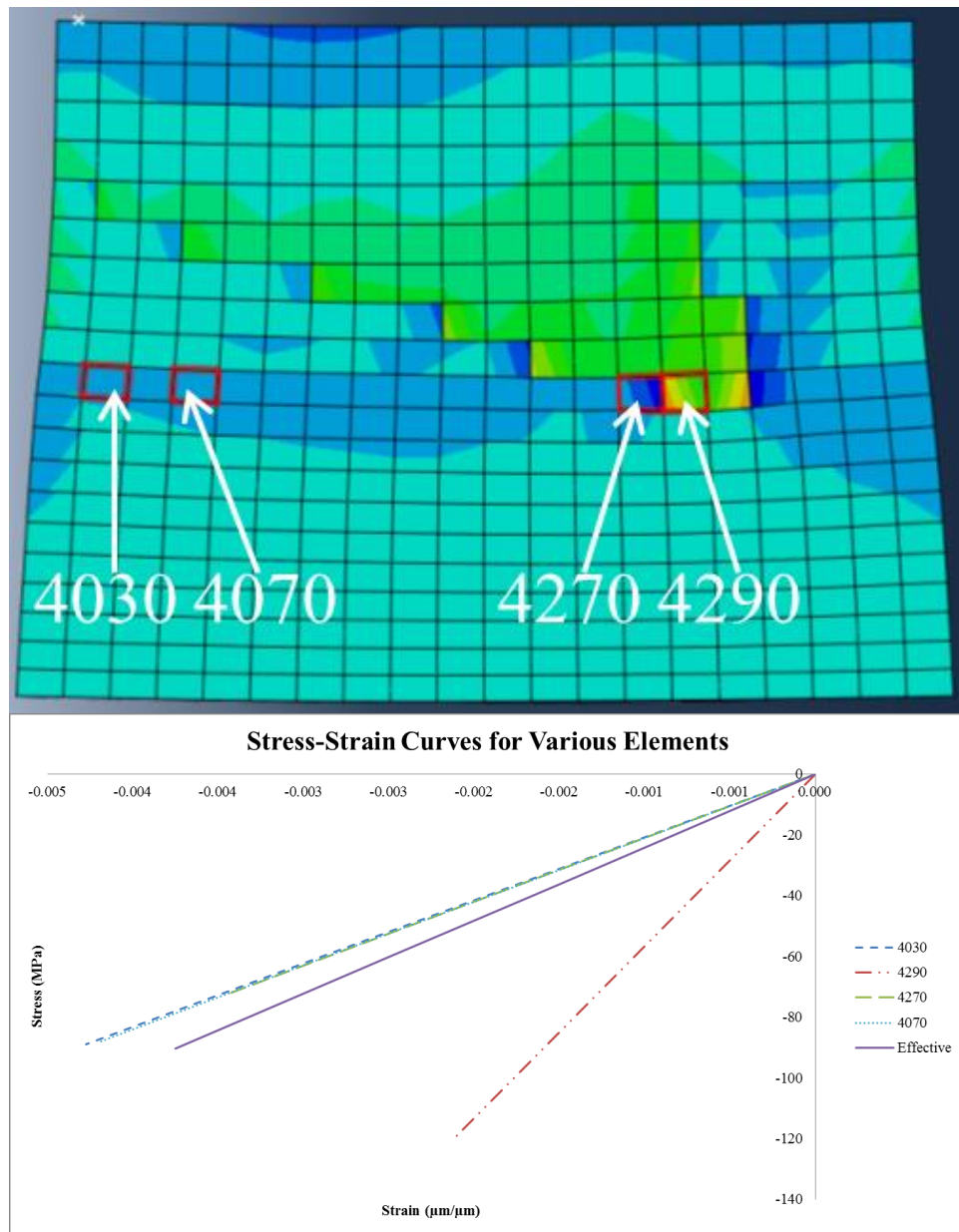


Figure 31: Stress-strain curves for various elements in the interface layer

A simplified elastic-perfectly plastic model was employed for all layers of the fish scale for initial investigations into material response to large strain conditions. To analyze the interfacial region a 160x160x160 μm model was incrementally loaded in tension up to strain of 1.3% using periodic boundary conditions. Results show significant energy dissipation through plastic deformation without increased stress in the ganoine layers. The bone layer appears to provide energy absorption while allowing the ganoine layer to maintain its structural integrity during large effective strain conditions.

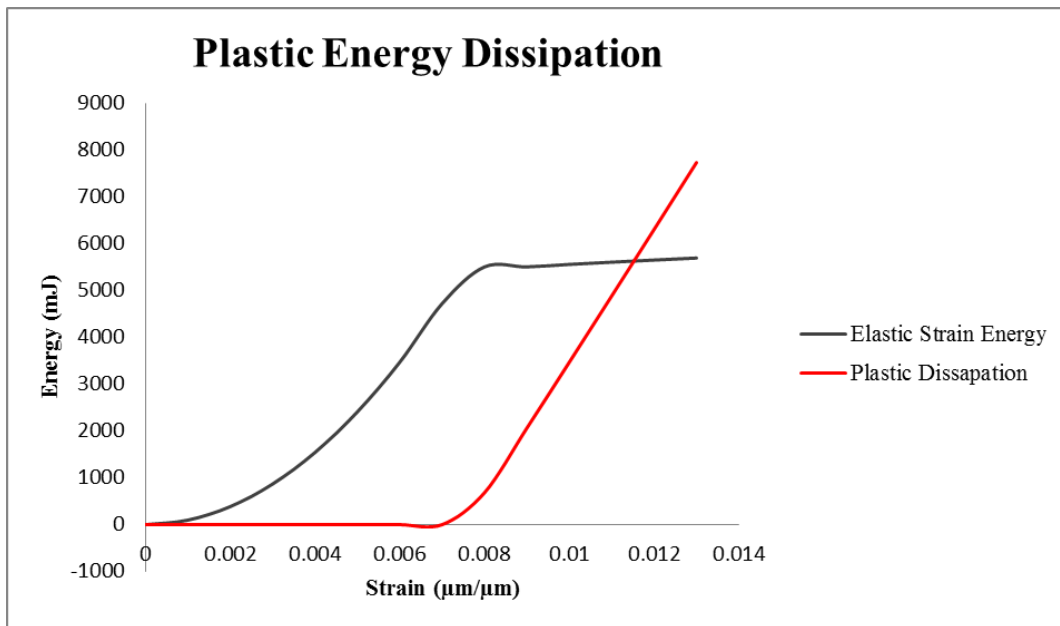


Figure 32: Plastic energy dissipation for single sawtooth model of Alligator gar interface

To determine the stress distribution due to compressive loading and the effects of the structured interface the one million element model and applied displacement up 1.3% average strain was simulated to ensure plastic deformation occurs, but is well below the reported failure strain. Simulation results show a complex stress state within the RVE and significant energy dissipation due to plastic deformation of the bone layer. As in the analysis of the interface the compliant bone layer plastically deforms and leaves the ganoine layer in a stress state (-110 MPa) well below its yield strength of 1.05 GPa (Figure 33).

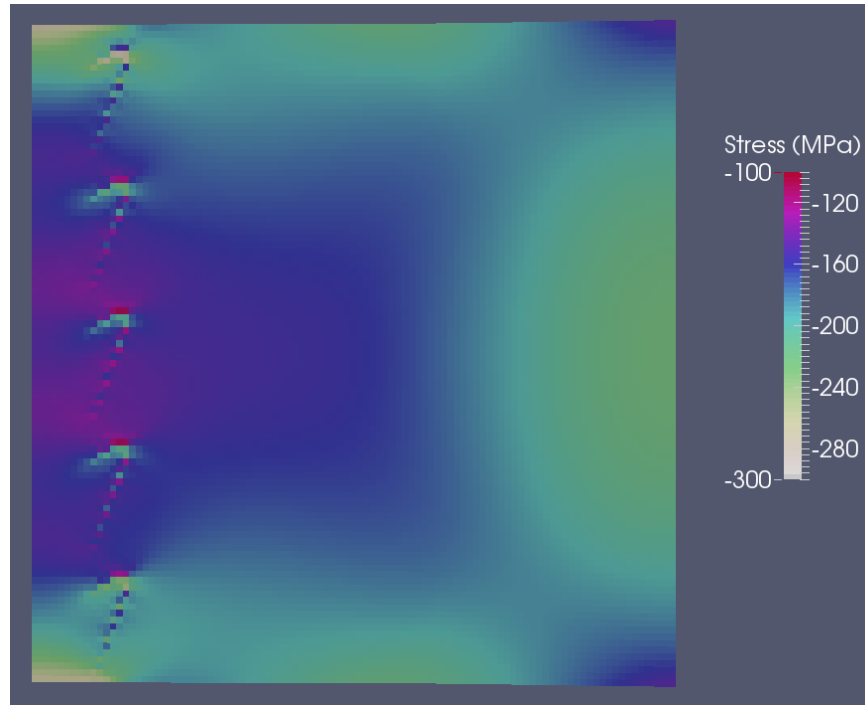


Figure 33: Elastic - perfectly plastic simulation results for the one million element RVE

As the RVE is loaded, plastic deformation occurs at 0.65% average strain and is 44% of the mechanical energy dissipated at 1.3% strain (Table 5). The plastic deformation only occurs in the bone layer while the ganoine layer exhibits only elastic deformation. The compliance of the bone layer allows for significant deformation without an increase the stress in the ganoine layer.

Table 5: Elastic and plastic energy dissipation

Strain ($\mu\text{m}/\mu\text{m}$)	% Elastic energy	% Plastic energy
0.0000	100	0
0.0033	100	0
0.0065	100	0
0.0114	68.21	31.79
0.0130	55.96	44.04

The plastic deformation progresses through the bone layer from the innermost surface towards the ganoine layer as loading occurs. Simulation results indicate plastic energy is the dissipation mechanism allowing for large RVE strains and leaving the ganoine layer to maintain its structural integrity through progressive yielding within the bone layer (Figure 34). While

damage initiation has not been considered to date, the current findings could indicate significant energy dissipative capabilities for a functionally graded composite with structured lamellar interfaces. Allowing for progressive yielding will allow for high strength ceramic materials in large strain conditions and maintain their structural integrity.

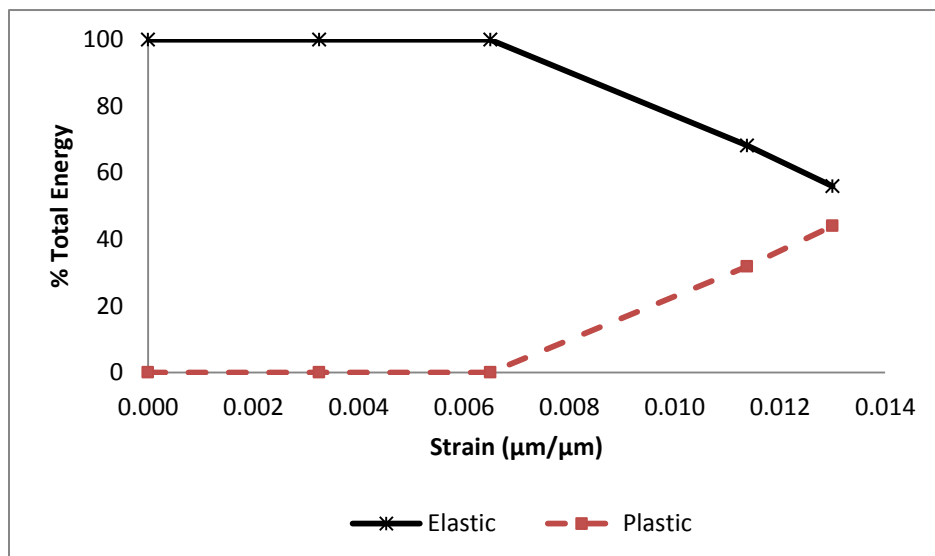


Figure 34: RVE energy dissipation during compression loading

CHAPTER 6

CONCLUSIONS AND FUTURE WORK

6.1 Conclusions

The RVE based approach has shown that is possible to determine the elastic properties for a functional graded, structurally anisotropic material systems. Simulation results show that the combination of both characteristics provide a anisotropic material response with a slight variation in the transverse modulus. In comparison with the traditional Voigt and Reuss bounds for composite material the elastic properties indicate stiffening due to the continuous gradation of elastic modulus as well as the sawtooth structure present at the interface.

Analysis of the Alligator gar fish scale RVE provided novel insight into the effects of a sawtooth structured interface. ABAQUS® FE simulation analysis indicates that the sawtooth structure provides stress localization allowing for a lower stress state to be present in the interfacial region. Under shear loading, which is of particular importance for delamination resistance, the compliant bone layer allows for significant deformation and energy absorption potentially indicating an increase in interfacial integrity for large strain conditions. The functional grading of material properties appears to preferential for longitudinal loading conditions indicated by a significantly lower stress state in the ganoine layer as compared to transverse loading conditions.

Under elastic – perfectly plastic compression simulations the bone layer provides significant plastic deformation and plastic energy dissipation while leaving the protective ganoine layer as stresses well below (100 – 160 MPa) the reported yield strength of 1.05 GPa. Provided the fish scale is under external predatory attack this would allow for large strains to be achieved before the ganoine layer is compromised.

6.2 Future Work

Future work will consist of increased complexity within the RVE to more accurately capture the distinct material behavior of the viscoelastic collagen fibers and brittle HAp as well as the hard-soft interface present between the outer ganoine and inner bone layer. Potential work will include microindentation modeling for validation versus current experimental characterization as well as capture the hydration effects on penetration resistance and large strain conditions.

In addition, the effects of high strain rate would be of interest due to the potential for improved force protection with structured interface lamellar composites. After completion of the biological material analysis the principals learned will be applied to bio-inspired novel design for an advanced soft and brittle composite material system.

LIST OF REFERENCES

- [1] Jeronimidis, G., & Atkins, A. G. (1995). Mechanics of biological materials and structures: Nature's lessons for the engineer. *Proceedings of the Institution of Mechanical Engineers, Part C: Journal of Mechanical Engineering Science*, 209(4), 221-235.
- [2] Song, J. (2011). Multiscale materials design of natural exoskeletons: fish armor (Doctoral dissertation, Massachusetts Institute of Technology).
- [3] Song, J., Ortiz, C., & Boyce, M. C. (2011). Threat-protection mechanics of an armored fish. *Journal of the mechanical behavior of biomedical materials*, 4(5), 699-712.
- [4] Tennyson, R. C., R. Ewert, and V. Niranjan. "Dynamic viscoelastic response of bone." *Experimental Mechanics* 12.11 (1972): 502-507
- [5] Ji, B., & Gao, H. (2010). Mechanical principles of biological nanocomposites. *Annual Review of Materials Research*, 40, 77-100.
- [6] Gao, H. (2004, Aug 17) Nanoscale Mechanics of Biological Materials. Gutkowski, W., & Kowalewski, TA. *ICTAM04 Abstracts and CD-ROM Proceedings*. Paper presented at 21st International Congress of Theoretical and Applied Mechanics. Retrieved from http://fluid.ippt.gov.pl/ictam04/text/sessions/docs/SL5/10772/SL5_10772.pdf
- [7] Sacks, M. S., & Sun, W. (2003). Multiaxial mechanical behavior of biological materials. *Annual review of biomedical engineering*, 5(1), 251-284.
- [8] Wu, M. S. (2011). Strategies and challenges for the mechanical modeling of biological and bio-inspired materials. *Materials Science and Engineering: C*, 31(6), 1209-1220.
- [9] Buehler, M. J., & Yung, Y. C. (2010). How protein materials balance strength, robustness, and adaptability. *HFSP journal*, 4(1), 26-40. McKittrick, J., Chen, P. Y., Tombolato, L., Novitskaya, E. E., Trim, M. W., Hirata, G. A., ... & Meyers, M. A. (2010). Energy absorbent natural materials and bioinspired design strategies: A review. *Materials Science and Engineering: C*, 30(3), 331-342.
- [10] Hamed, E., & Jasiuk, I. (2012). Elastic modeling of bone at nanostructural level. *Materials Science and Engineering: R: Reports*, 73(3), 27-49.
- [11] Martin, R. B. (1983). Porosity and specific surface of bone. *Critical reviews in biomedical engineering*, 10(3), 179-222
- [12] Buehler, M. J., Yao, H., Ji, B., & Gao, H. (2005). Atomistic and continuum studies of flaw tolerant nanostructures in biological systems. In *MATERIALS RESEARCH SOCIETY SYMPOSIUM PROCEEDINGS* (Vol. 844, p. 207). Warrendale, Pa.; Materials Research Society; 1999.
- [13] Katti, K. S., Turlapati, P., Verma, D., Bhowmik, R., Gujjula, P. K., & Katti, D. R. (2006). Static and dynamic mechanical behavior of hydroxyapatite-polyacrylic acid composites under simulated body fluid. *American Journal of Biochemistry and Biotechnology*, 2(2), 73.
- [14] Meyers, M. A., Lin, A. Y., Seki, Y., Chen, P. Y., Kad, B. K., & Bodde, S. (2006). Structural biological composites: an overview. *Jom*, 58(7), 35-41.
- [15] Gupta, H. S., Wagermaier, W., Zickler, G. A., Raz-Ben Aroush, D., Funari, S. S., Roschger, P., ... & Fratzl, P. (2005). Nanoscale deformation mechanisms in bone. *Nano Letters*, 5(10), 2108-2111.
- [16] Gupta, H. S., Seto, J., Wagermaier, W., Zaslansky, P., Boesecke, P., & Fratzl, P. (2006). Cooperative deformation of mineral and collagen in bone at the nanoscale. *Proceedings of the National Academy of Sciences*, 103(47), 17741-17746.

- [17] Gupta, H. S., Wagermaier, W., Zickler, G. A., Hartmann, J., Funari, S. S., Roschger, P., ... & Fratzl, P. (2006). Fibrillar level fracture in bone beyond the yield point. *International journal of fracture*, 139(3-4), 425-436.
- [18] Gao, H. (2006). Application of fracture mechanics concepts to hierarchical biomechanics of bone and bone-like materials. *International Journal of Fracture*, 138(1-4), 101-137.
- [19] Gao, H., & Ji, B. (2004, January). Modeling fracture in nano materials. In *IUTAM Symposium on Asymptotics, Singularities and Homogenisation in Problems of Mechanics* (pp. 307-316). Springer Netherlands.
- [20] Gao, H., Ji, B., Buehler, M. J., & Yao, H. (2004). Flaw tolerant bulk and surface nanostructures of biological systems. *Mech. Chem. Biosyst*, 1(1), 37-52.
- [21] Dubey, D. K., & Tomar, V. (2010). Role of molecular level interfacial forces in hard biomaterial mechanics: a review. *Annals of biomedical engineering*, 38(6), 2040-2055.
- [22] Buehler, M. J. (2007). Nano-and micromechanical properties of hierarchical biological materials and tissues. *Journal of Materials Science*, 42(21), 8765-8770.
- [23] Ritchie, R. O., Buehler, M. J., & Hansma, P. (2009). Plasticity and toughness in bone. *Phys Today*, 62(6), 41-47.
- [24] Dimas, L. S., & Buehler, M. J. (2012). Influence of geometry on mechanical properties of bio-inspired silica-based hierarchical materials. *Bioinspiration & biomimetics*, 7(3), 036024.
- [25] Espinosa, H. D., Rim, J. E., Barthelat, F., & Buehler, M. J. (2009). Merger of structure and material in nacre and bone—Perspectives on *de novo* biomimetic materials. *Progress in Materials Science*, 54(8), 1059-1100.
- [26] Schönbörner, A. A., Boivin, G., & Baud, C. A. (1979). The mineralization processes in teleost fish scales. *Cell and tissue research*, 202(2), 203-212.
- [27] Ikoma, T., Kobayashi, H., Tanaka, J., Walsh, D., & Mann, S. (2003). Microstructure, mechanical, and biomimetic properties of fish scales from *Pagrus major*. *Journal of Structural Biology*, 142(3), 327-333.
- [28] Ikoma, T., Kobayashi, H., Tanaka, J., Walsh, D., & Mann, S. (2003). Physical properties of type I collagen extracted from fish scales of *Pagrus major* and *Oreochromis niloticus*. *International journal of biological macromolecules*, 32(3), 199-204.
- [29] Zhu, D., Ortega, C. F., Motamedi, R., Szewciw, L., Vernerey, F., & Barthelat, F. (2012). Structure and mechanical performance of a “modern” fish scale. *Advanced Engineering Materials*, 14(4), B185-B194.
- [30] Youn, H. S., & Shin, T. J. (2009). Supramolecular assembly of collagen fibrils into collagen fiber in fish scales of red seabream, *Pagrus major*. *Journal of structural biology*, 168(2), 332-336.
- [31] Bruet, B. J., Song, J., Boyce, M. C., & Ortiz, C. (2008). Materials design principles of ancient fish armour. *Nature materials*, 7(9), 748-756.
- [32] Vernerey, F. J., & Barthelat, F. (2010). On the mechanics of fishscale structures. *International Journal of Solids and Structures*, 47(17), 2268-2275.
- [33] Allison, Paul G., et al. "Mechanical properties and structure of the biological multilayered material system, *Atractosteus spatula* scales." *Acta biomaterialia* (2012).
- [34] Yang, Wen, et al. "Structure and fracture resistance of alligator gar (*Atractosteus spatula*) armored fish scales." *Acta biomaterialia* (2013).
- [35] Yang, W., Chen, I. H., Mckittrick, J., & Meyers, M. A. (2012). Flexible Dermal Armor in Nature. *JOM*, 64(4), 475-485.

- [36] Chen, P. Y., Schirer, J., Simpson, A., Nay, R., Lin, Y. S., Yang, W., ... & Meyers, M. A. (2012). Predation versus protection: fish teeth and scales evaluated by nanoindentation. *Journal of Materials Research*, 27(1), 100.
- [37] Han, L., Wang, L., Song, J., Boyce, M. C., & Ortiz, C. (2011). Direct quantification of the mechanical anisotropy and fracture of an individual exoskeleton layer via uniaxial compression of micropillars. *Nano letters*, 11(9), 3868-3874.
- [38] Yang, W., Gludovatz, B., Zimmermann, E. A., Bale, H. A., Ritchie, R. O., & Meyers, M. A. (2013). Structure and fracture resistance of alligator gar (*Atractosteus spatula*) armored fish scales. *Acta biomaterialia*, 9(4), 5876-5889.
- [39] Yang, W., Chen, I. H., Gludovatz, B., Zimmermann, E. A., Ritchie, R. O., & Meyers, M. A. (2013). Natural flexible dermal armor. *Advanced Materials*, 25(1), 31-48.
- [40] Qi, H. J., Ortiz, C., & Boyce, M. C. (2006). Mechanics of biomacromolecular networks containing folded domains. *Transactions-American Society of Mechanical Engineers Journal of Engineering Materials And Technology*, 128(4), 509.
- [41] Vernerey, F. J., & Barthelat, F. (2010). On the mechanics of fishscale structures. *International Journal of Solids and Structures*, 47(17), 2268-2275.
- [42] Browning, A., Ortiz, C., & Boyce, M. C. (2012). Mechanics of composite elasmoid fish scale assemblies and their bioinspired analogues. *Journal of the Mechanical Behavior of Biomedical Materials*, 19, 75 – 86.
- [43] Chandler, M. Q., Allison, P. G., Rodriguez, R. I., Moser, R. D., & Kennedy, A. J. (2014). Finite element modeling of multilayered Structures of fish Scales. *Journal of the mechanical behavior of biomedical materials*.
- [44] Ehlers, W., Karajan, N., & Markert, B. (2006). A porous media model describing the inhomogeneous behaviour of the human intervertebral disc. *Materialwissenschaft und Werkstofftechnik*, 37(6), 546-551.
- [45] Shuchun, Z., & Yueguang, W. (2007). Effective elastic modulus of bone-like hierarchical materials. *Acta Mechanica Solida Sinica*, 20(3), 198-205.
- [46] Barkaoui, A., & Hambli, R. (2011). *Finite element 3D modeling of mechanical behavior of mineralized collagen microfibrils*. arXiv preprint arXiv:1112.0984.
- [47] Barkaoui, A., & Hambli, R. (2011). 3D Multiscale Modelling of Cortical Bone Structure, Using the Inverse Identification Method: Microfibril Scale Study. arXiv preprint arXiv:1112.0984.
- [48] Alexander, T., Antonis, L., Savvas, S., & Nikolaos, M. (2012). Nonintrusive 3D reconstruction of human bone models to simulate their bio-mechanical response. *3D Research*, 3(2), 1-10.
- [49] Carretta, R., Lorenzetti, S., & Müller, R. (2012). Towards patient-specific material modeling of trabecular bone post-yield behavior. *International journal for numerical methods in biomedical engineering*.
- [50] Tai, K., Dao, M., Suresh, S., Palazoglu, A., & Ortiz, C. (2007). Nanoscale heterogeneity promotes energy dissipation in bone. *Nature materials*, 6(6), 454-462
- [51] Akiva, U., Wagner, H. D., & Weiner, S. (1998). Modelling the three-dimensional elastic constants of parallel-fibred and lamellar bone. *Journal of Materials Science*, 33(6), 1497-1509.
- [52] Tang, Y., Ballarini, R., Buehler, M. J., & Eppell, S. J. (2010). Deformation micromechanisms of collagen fibrils under uniaxial tension. *Journal of The Royal Society Interface*, 7(46), 839-850.

- [53] Bar-On, B., & Wagner, H. D. (2011). Mechanical model for staggered bio-structure. *Journal of the Mechanics and Physics of Solids*, 59(9), 1685-1701.
- [54] Hollister, S. J., & Kikuchi, N. (1994). Homogenization theory and digital imaging: a basis for studying the mechanics and design principles of bone tissue. *Biotechnology and bioengineering*, 43(7), 586-596.
- [55] Fritsch A., Hellmich, C., & Young, P. (2011, Feb. 16-18) Porosity-Dependent Elasticity AND Strength of Ceramic Bone Biomaterials: Micromechanics-Based Assessment of Power Functions. Baumgartner, C. *Biomedical Engineering – 2011*. Paper presented at IASTED International Conference: Bimedical Engineering, Innsbruck, Austria. Online: Actapress.
- [56] Ritchie, R. O., Kinney, J. H., Kruzic, J. J., & Nalla, R. K. (2005). A fracture mechanics and mechanistic approach to the failure of cortical bone. *Fatigue & Fracture of Engineering Materials & Structures*, 28(4), 345-371.
- [57] Chao, E. Y., Volokh, K. Y., Yoshida, H., Shiba, N., & Ide, T. (2010). Discrete element analysis in musculoskeletal biomechanics. *Molecular & cellular biomechanics: MCB*, 7(3), 175.
- [58] Doll, K., & Ural, A. (2013). Mechanical Evaluation of Hydroxyapatite Nanocomposites Using Finite Element Modeling. *Journal of Engineering Materials and Technology*, 135(1), 011007.
- [59] Buehler, M. J. (2007). Molecular nanomechanics of nascent bone: fibrillar toughening by mineralization. *Nanotechnology*, 18(29), 295102.
- [60] Qin, Z., Gautieri, A., Nair, A. K., Inbar, H., & Buehler, M. J. (2012). Thickness of Hydroxyapatite Nanocrystal Controls Mechanical Properties of the Collagen–Hydroxyapatite Interface. *Langmuir*, 28(4), 1982-1992.
- [61] Libonati, F., Nair, A. K., Vergani, L., & Buehler, M. J. (2013). Fracture mechanics of hydroxyapatite single crystals under geometric confinement. *Journal of the mechanical behavior of biomedical materials*, 20, 184-191.
- [62] Zamiri, A., & De, S. (2011). Mechanical properties of hydroxyapatite single crystals from nanoindentation data. *Journal of the mechanical behavior of biomedical materials*, 4(2), 146-152.
- [63] Ching, W. Y., Rulis, P., & Misra, A. (2009). Ab initio elastic properties and tensile strength of crystalline hydroxyapatite. *Acta Biomaterialia*, 5(8), 3067-3075.
- [64] Hambli, R., & Barkaoui, A. (2012). Physically based 3D finite element model of a single mineralized collagen microfibril. *Journal of Theoretical Biology*, 301, 28-41.
- [65] Gautieri, A., Vesentini, S., Redaelli, A., & Buehler, M. J. (2012). Viscoelastic properties of model segments of collagen molecules. *Matrix Biology*, 31(2), 141-149.
- [66] Tang, H., Buehler, M. J., & Moran, B. (2009). A constitutive model of soft tissue: from nanoscale collagen to tissue continuum. *Annals of biomedical engineering*, 37(6), 1117-1130.
- [67] Hadi, M. F., & Barocas, V. H. (2013). Microscale Fiber Network Alignment Affects Macroscale Failure Behavior in Simulated Collagen Tissue Analogs. *Journal of biomechanical engineering*, 1, 545.
- [68] Fantner, G. E., Hassenkam, T., Kindt, J. H., Weaver, J. C., Birkedal, H., Pechenik, L., ... & Hansma, P. K. (2005). Sacrificial bonds and hidden length dissipate energy as mineralized fibrils separate during bone fracture. *Nature Materials*, 4(8), 612-616.

- [69] Buehler, M. J. (2006). Nature designs tough collagen: explaining the nanostructure of collagen fibrils. *Proceedings of the National Academy of Sciences*, 103(33), 12285-12290.
- [70] Buehler, M. J., & Wong, S. Y. (2007). Entropic elasticity controls nanomechanics of single tropocollagen molecules. *Biophysical journal*, 93(1), 37-43.
- [71] Buehler, M. J. (2008). Molecular architecture of collagen fibrils: a critical length scale for tough fibrils. *Current Applied Physics*, 8(3), 440-442.
- [72] Gautieri, A., Buehler, M. J., & Redaelli, A. (2009). Deformation rate controls elasticity and unfolding pathway of single tropocollagen molecules. *Journal of the Mechanical Behavior of Biomedical Materials*, 2(2), 130-137.
- [73] Gautieri, A., Vesentini, S., Redaelli, A., & Buehler, M. J. (2011). Hierarchical structure and nanomechanics of collagen microfibrils from the atomistic scale up. *Nano letters*, 11(2), 757-766.
- [74] Buehler, M. J. (2009). Defining Nascent Bone by the Molecular Nanomechanics of Mineralized Collagen Fibrils. *ASME*.
- [75] Nair, A. K., Gautieri, A., Chang, S. W., & Buehler, M. J. (2013). Molecular mechanics of mineralized collagen fibrils in bone. *Nature communications*, 4, 1724.
- [76] Marko, J. F., & Siggia, E. D. (1995). Stretching DNA. *Macromolecules*, 28(26), 8759-8770.
- [77] Buehler, M. J., & Ackbarow, T. (2007). Fracture mechanics of protein materials. *Materials Today*, 10(9), 46-58.
- [78] Gautieri, A., Vesentini, S., Montevecchi, F. M., & Redaelli, A. (2008). Mechanical properties of physiological and pathological models of collagen peptides investigated via steered molecular dynamics simulations. *Journal of biomechanics*, 41(14), 3073-3077.
- [79] Almora-Barrios, N., Austen, K. F., & de Leeuw, N. H. (2009). Density functional theory study of the binding of glycine, proline, and hydroxyproline to the hydroxyapatite (0001) and (0110) surfaces. *Langmuir*, 25(9), 5018-5025.
- [80] Buehler, M. J. (2006). Mechanics of protein crystals: Atomistic modeling of elasticity and fracture. *Journal of Computational and Theoretical Nanoscience*, 3(5), 670-683.
- [81] Katz, J. L., Misra, A., Spencer, P., Wang, Y., Bumrerraj, S., Nomura, T., ... & Tabib-Azar, M. (2007). Multiscale mechanics of hierarchical structure/property relationships in calcified tissues and tissue/material interfaces. *Materials Science and Engineering: C*, 27(3), 450-468.
- [82] Andrade, J. E., Avila, C. F., Hall, S. A., Lenoir, N., & Viggiani, G. (2011). Multiscale modeling and characterization of granular matter: from grain kinematics to continuum mechanics. *Journal of the Mechanics and Physics of Solids*, 59(2), 237-250.
- [83] Pradhan, S. M., Katti, K. S., & Katti, D. R. (2012). A Multiscale Model of Collagen Fibril in Bone: Elastic Response. *Journal of Engineering Mechanics*.
- [84] Hatami-Marbini, H., Shahsavari, A., & Picu, R. C. (2013). Multiscale modeling of semiflexible random fibrous structures. *Computer-Aided Design*, 45(1), 77-83.
- [85] Elliot, J. (1/18/2007). Modeling across different time and length scales: An introduction to multiscale modelling and mesoscale methods. Course lecture. University of Cambridge, Cambridge, UK.
- [86] Buehler, M. J. (2006). Atomistic and continuum modeling of mechanical properties of collagen: elasticity, fracture, and self-assembly. *Journal of Materials Research*, 21(08), 1947-1961.

- [87] Buehler, M. J. (2006). Large-scale hierarchical molecular modeling of nanostructured biological materials. *Journal of Computational and Theoretical Nanoscience*, 3(5), 603-623.
- [88] Buehler, M. J. (2008). Nanomechanics of collagen fibrils under varying cross-link densities: atomistic and continuum studies. *Journal of the Mechanical Behavior of Biomedical Materials*, 1(1), 59-67.
- [89] Buehler, M. J., & Ackbarow, T. (2008). Nanomechanical strength mechanisms of hierarchical biological materials and tissues. *Computer Methods in Biomechanics and Biomedical Engineering*, 11(6), 595-607.
- [90] Buehler, M. J. (2010). Multiscale mechanics of biological and biologically inspired materials and structures. *Acta Mechanica Solida Sinica*, 23(6), 471-483.
- [91] Buehler, M. J. (2011). Multiscale aspects of mechanical properties of biological materials. *Journal of the Mechanical Behavior of Biomedical Materials*, 4(2), 125-127.
- [92] Saber-Samandari, S., & Gross, K. A. (2009). Micromechanical properties of single crystal hydroxyapatite by nanoindentation. *Acta Biomaterialia*, 5(6), 2206-2212.
- [93] Rupin, F., Saied, A., Dalmas, D., Peyrin, F., Hauptert, S., Barthel, E., ... & Laugier, P. (2008). Experimental determination of Young modulus and Poisson ratio in cortical bone tissue using high resolution scanning acoustic microscopy and nanoindentation. *The Journal of the Acoustical Society of America*, 123(5), 3785-3785.
- [94] Shahzamanian, M. M., Tadepalli, T., Rajendran, A. M., Hodo, W. D., Mohan, R., Valisetty, R., ... & Ramsey, J. J. (2014). Representative Volume Element Based Modeling of Cementitious Materials. *Journal of Engineering Materials and Technology*, 136(1), 011007.

LIST OF APPENDICES

APPENDIX A: PYTHON SCRIPT FOR ABAQUS ODB FILE

ABAQUS® ODB file post processing script

```
import sys
from abaqus import*
from abaqusConstants import*
from odbAccess import*
import visualization
import xyPlot

myOdb = session.openOdb(name='C:/temp/garKBCplanar.odb')

#Open VTK Legacy file for energy data
vtkFile = open('E11PEnergyKBC.vtk', 'w')
vtkFile.write('# vtk DataFile Version 4.2\n')
vtkFile.write('Alligator Gar RVE Energy\n')
vtkFile.write('ASCII\n')
vtkFile.write('DATASET UNSTRUCTURED_GRID\n')

#Open VTK Legacy file for stress tensor data
vtkFile2 = open('E11PStressKBC.vtk', 'w')
vtkFile2.write('# vtk DataFile Version 4.2\n')
vtkFile2.write('Alligator Gar RVE Stress\n')
vtkFile2.write('ASCII\n')
vtkFile2.write('DATASET UNSTRUCTURED_GRID\n')

#Open VTK Legacy file for strain tensor data
vtkFile3 = open('E11PStrainKBC.vtk', 'w')
vtkFile3.write('# vtk DataFile Version 4.2\n')
vtkFile3.write('Alligator Gar RVE Strain\n')
vtkFile3.write('ASCII\n')
vtkFile3.write('DATASET UNSTRUCTURED_GRID\n')

#Display analyzed RVE in the ABAQUS Viewport
session.viewports['Viewport: 1'].setValues(displayedObject=myOdb)
myAssembly = myOdb.rootAssembly

ref_node = 2

#Define FE model information and last frame
instanceName = 'PART-1-1'
stepName = 'STEP-1'
lastFrame = myOdb.steps[stepName].frames[-1]

# Isolate the instance, get the number of nodes and elements
myInstance = myOdb.rootAssembly.instances[instanceName]
numNodes = len(myInstance.nodes)
```

```

numElements = len(myInstance.elements)
print numNodes
print numElements

frames = myOdb.steps[stepName].frames

#Write number of points to VTK Legacy file
vtkFile.write('POINTS %i float\n' % (numNodes))
vtkFile2.write('POINTS %i float\n' % (numNodes))
vtkFile3.write('POINTS %i float\n' % (numNodes))

# Isolate the displacement field
displacements = lastFrame.fieldOutputs['U'].getSubset(region=myInstance).values

# Determine initial nodal coordinates in XYZ space
initialCoords = []
for nd in range(0, numNodes):
    coords = myInstance.nodes[nd].coordinates
    initialCoords.append((coords[0], coords[1], coords[2]))

print nd

# Determine nodes that define hexahadron connectivity
elementConnectivity = []
for el in range(0, numElements):
    con = myInstance.elements[el].connectivity
    elementConnectivity.append(con)

# Add displacements to the initial coordinates
for nd in range(0, numNodes):
    x = initialCoords[nd][0]+displacements[nd].data[0]
    y = initialCoords[nd][1]+displacements[nd].data[1]
    z = initialCoords[nd][2]+displacements[nd].data[2]

# Write coordinates for deformed RVE to VTK Legacy file
vtkFile.write("\n%f %f %f" % (x,y,z))
vtkFile2.write("\n%f %f %f" % (x,y,z))
vtkFile3.write("\n%f %f %f" % (x,y,z))

# Write the number of elements to the VTK Legacy file
vtkFile.write("\n\nCELLS %i %i\n" % (numElements, 9*numElements))
vtkFile2.write("\n\nCELLS %i %i\n" % (numElements, 9*numElements))
vtkFile3.write("\n\nCELLS %i %i\n" % (numElements, 9*numElements))
for el in range(0,numElements):
    n1 = elementConnectivity[el][0]-1 #subtract 1 to for paraview number scheme
    n2 = elementConnectivity[el][1]-1

```

```

n3 = elementConnectivity[el][2]-1
n4 = elementConnectivity[el][3]-1
n5 = elementConnectivity[el][4]-1
n6 = elementConnectivity[el][5]-1
n7 = elementConnectivity[el][6]-1
n8 = elementConnectivity[el][7]-1

# Write element connectivity matrix to VTK Legacy file format
vtkFile.write('8 %i %i %i %i %i %i %i %i\n' % (n1, n2, n3, n4, n5, n6, n7, n8))
vtkFile2.write('8 %i %i %i %i %i %i %i %i\n' % (n1, n2, n3, n4, n5, n6, n7, n8))
vtkFile3.write('8 %i %i %i %i %i %i %i %i\n' % (n1, n2, n3, n4, n5, n6, n7, n8))

# Define element type; 12 = hexahadron
vtkFile.write('\nCELL_TYPES %i\n' % (numElements))
vtkFile2.write('\nCELL_TYPES %i\n' % (numElements))
vtkFile3.write('\nCELL_TYPES %i\n' % (numElements))
for el in range(0,numElements):
    vtkFile.write('12\n')
    vtkFile2.write('12\n')
    vtkFile3.write('12\n')

# For each displacement value, print the nodeLabel
# and data members.

##outputFile = open('outputs_strain1.dat','w')
##outputFile2 = open('outputs_stress1.dat','w')

# Define parameters as cell data
vtkFile.write('\nCELL_DATA %i' % (numElements))
vtkFile2.write('\nCELL_DATA %i' % (numElements))
vtkFile3.write('\nCELL_DATA %i' % (numElements))

# Print out the stress tensor field to the vtk file
vtkFile2.write('\nTENSORS stress float\n')
vtkFile3.write('\nTENSORS strain float\n')

# Scalar table for cell energy
vtkFile.write('\nSCALARS Energy float\n')
vtkFile.write('LOOKUP_TABLE default\n')

#Determine average stress in a given element
#for s in fieldOutput2:
for el in range(0,numElements):
    # Define field values to extract from ABAQUS ODB file. S = stress; E = strain

```

```

fieldValues2 = lastFrame.fieldOutputs['S'].getSubset(region=myInstance.elements[e1]).values
fieldValues = lastFrame.fieldOutputs['E'].getSubset(region=myInstance.elements[e1]).values

```

```

# Set each elements initial energy, stain and stress to zero

```

```

energy = 0.0

```

```

E11 = 0.0

```

```

E22 = 0.0

```

```

E33 = 0.0

```

```

E12 = 0.0

```

```

E13 = 0.0

```

```

E23 = 0.0

```

```

S11 = 0.0

```

```

S22 = 0.0

```

```

S33 = 0.0

```

```

S12 = 0.0

```

```

S13 = 0.0

```

```

S23 = 0.0

```

```

for ip in range(0,8):

```

```

    # Sum integration point strains and stress within an element

```

```

    E11 = E11+fieldValues[ip].data[0]*10000000000

```

```

    E22 = E22+fieldValues[ip].data[1]*10000000000

```

```

    E33 = E33+fieldValues[ip].data[2]*10000000000

```

```

    E12 = E12+fieldValues[ip].data[3]*10000000000

```

```

    E13 = E13+fieldValues[ip].data[4]*10000000000

```

```

    E23 = E23+fieldValues[ip].data[5]*10000000000

```

```

    S11 = S11+fieldValues2[ip].data[0]*10000000000

```

```

    S22 = S22+fieldValues2[ip].data[1]*10000000000

```

```

    S33 = S33+fieldValues2[ip].data[2]*10000000000

```

```

    S12 = S12+fieldValues2[ip].data[3]*10000000000

```

```

    S13 = S13+fieldValues2[ip].data[4]*10000000000

```

```

    S23 = S23+fieldValues2[ip].data[5]*10000000000

```

```

# Determine average strains in an element

```

```

E11_avg = E11/float(8)

```

```

E22_avg = E22/float(8)

```

```

E33_avg = E33/float(8)

```

```

E12_avg = E12/float(8)

```

```

E13_avg = E13/float(8)

```

```

E23_avg = E23/float(8)

```

```

S11_avg = S11/float(8)

```

```

# Determine average stresses in an element

```

```

S22_avg = S22/float(8)

```

```

S33_avg = S33/float(8)

```

```

S12_avg = S12/float(8)
S13_avg = S13/float(8)
S23_avg = S23/float(8)

# Calculate energy and write it to VTK Legacy file scalar lookup table
energy =
0.5*(S11_avg*E11_avg+S22_avg*E22_avg+S33_avg*E33_avg+S12_avg*E12_avg+S13_avg*
E13_avg+S23_avg*E23_avg)*10000
vtkFile.write('%f\n' % (energy))

# Write element stress tensor to VTK Legacy file
vtkFile2.write("\n%f %f %f % (S11_avg,S12_avg,S13_avg))
vtkFile2.write("\n%f %f %f % (S12_avg,S22_avg,S23_avg))
vtkFile2.write("\n%f %f %f % (S13_avg,S23_avg,S33_avg))
vtkFile2.write("\n")

# Write element strain tensor to VTK Legacy file
vtkFile3.write("\n%f %f %f % (E11_avg,E12_avg,E13_avg))
vtkFile3.write("\n%f %f %f % (E12_avg,E22_avg,E23_avg))
vtkFile3.write("\n%f %f %f % (E13_avg,E23_avg,E33_avg))
vtkFile3.write("\n")

#outputFile2.write('%2.10E %2.10E %2.10E %2.10E %2.10E %2.10E\n' % (S11, S22, S33,
S12, S13, S23))
##outputFile.close()
##outputFile2.close()

# Clean up
vtkFile.close()
vtkFile2.close()
vtkFile3.close()
myOdb.close()

```

APPENDIX B: PARAVIEW STRESS PLOTS

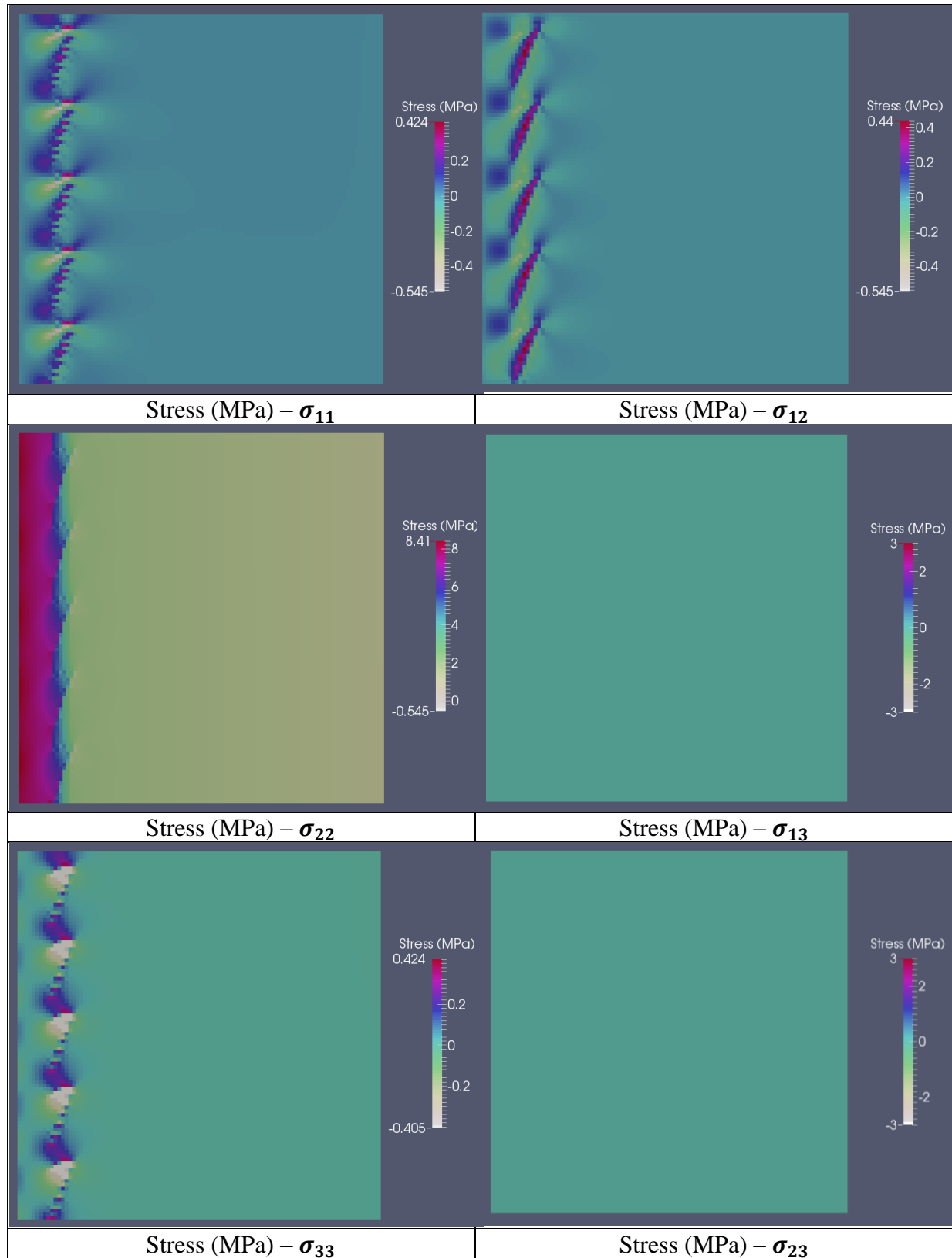


Figure 35: RVE stress distribution under uniaxial displacement condition (u_{22})

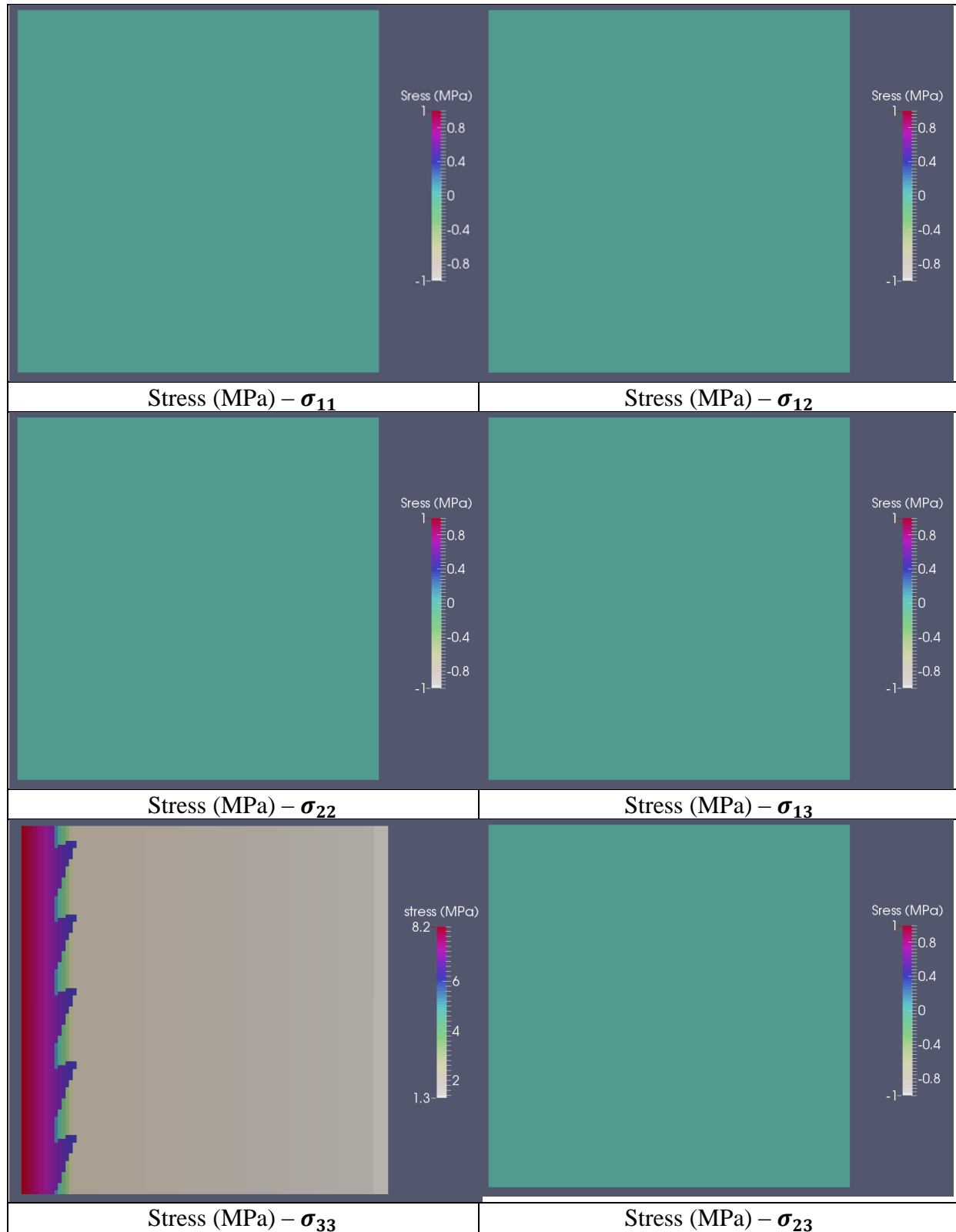


Figure 36: RVE stress distribution under uniaxial displacement condition (u_{33})

APPENDIX C: ABAQUS® SCALABILITY

ABAQUS® scalability tests were run to determine the effects of increased processors on the MCSR Sequoia system. The tests were performed up to eight processors on two nodes. Table 6 related the total CPU time to CPU hours preprocessor and the resulting efficiency of parallelization of ABAQUS FEA code for one million voxel elements. Each element has 8 nodes and three degrees of freedom (DOF) totaling over 24 million DOF for computation.

Table 6: ABAQUS® Scalability for one million element Alligator gar RVE

ABAQUS® scalability	MCSR	Sequoia	1x10 ⁶ elements	DOF: 24x10 ⁶	
number of cores	Total CPU time (s)	Time per processor (s)	CPU hours/ processor	ideal (hrs)	% Deviation
1	25093	25093	6.97	6.97	Reference
2	25514	12757	3.54	3.49	1.68
4	27485	6871.25	1.91	1.74	9.53
6	29901	4983.5	1.38	1.16	19.16

Figure 37 is the CPU hours per processor compared with the ideal scaling per processor showing a significant deviation and increases from 1.68% at two processors to 19.16% for six processors.

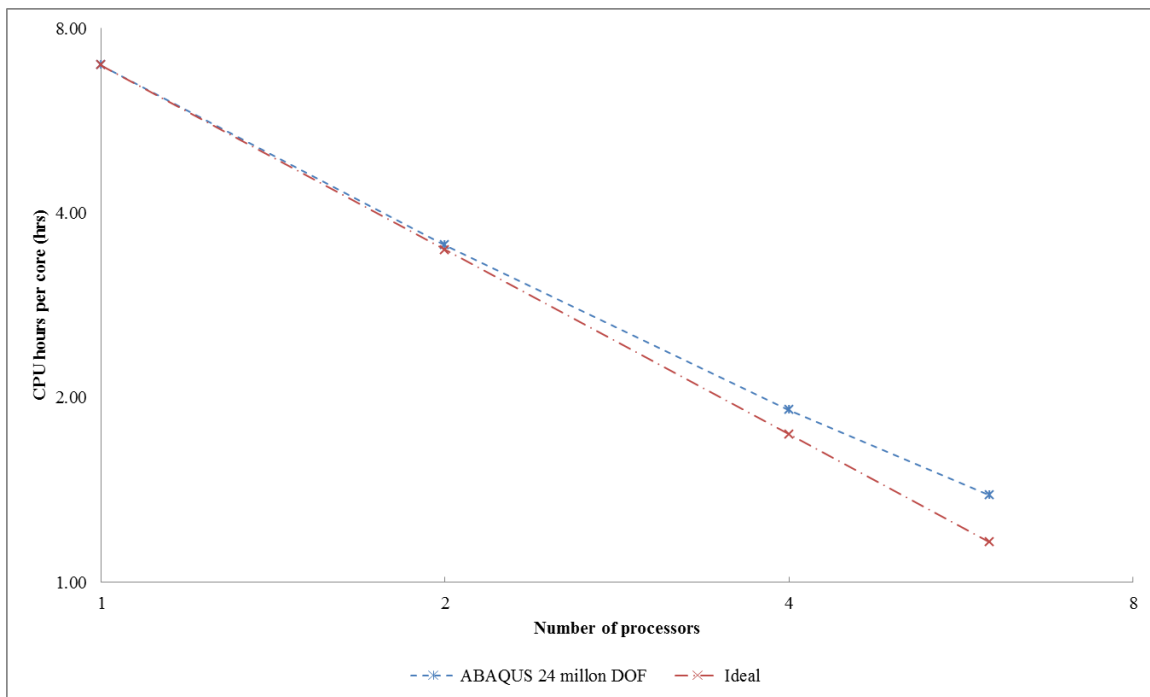


Figure 37: ABAQUS® scalability versus ideal for one million element RVE

The MCSR Sequoia system is a 124 node cluster with Altix XE 310, Altix XE320 and Rackable computing nodes. The Altix nodes contain Dual Intel Xeon Quad-core E5420 Harpertown processors and the Rackable nodes contain two six-core Intel Xeon X5650 (Westmere processors) and an Infiniband network card.

VITA

Matthew Nelms obtained his Bachelor of Science in Mechanical Engineering from the University of Colorado at Boulder in 2008 where he performed undergraduate research studying particle agglomeration on the free surface of a parametric excited fluid under Dr. Patrick Weidman.

He started at The University of Mississippi in August of 2011 working towards a Master of Science in Engineering Science with an emphasis in Mechanical Engineering. During his time at The University of Mississippi he conducted research into the experimental characterization of composite materials, been an graduate instructor teaching the undergraduate materials science laboratory course. During the 2012 – 2013 academic year he worked as a Graduate Fellow at The University of Mississippi's Center for Mathematics and Science Education aiding the implementation of two high school STEM competitions, The Real World Design Challenge and FIRST Tech Challenge.

He has conducted his thesis research under the guidance of Dr. A.M Rajendran focusing on biological material modeling for bio-inspired design principles. During the 2014 – 2015 academic year he has been awarded the NASA Mississippi Space Grant Graduate Fellowship. He will be continuing his education to obtain his PhD as well as his research into biomaterials and bio-inspired design under his advisor Dr. Rajendran in January 2015.